11-16-2020

Reduced-order Model Predictions of Wind Turbines via Mode Decomposition and Sparse Sampling

Ala' Eyad Qatramez

REDUCED-ORDER MODEL PREDICTIONS OF WIND TURBINES VIA MODE DECOMPOSITION AND SPARSE SAMPLING

by

Ala' Eyad Qatramez

A Thesis

Submitted in Partial Fulfillment of the

Requirements for the Degree of

Master of Science

Major: Mechanical Engineering

University of Memphis

December 2020

Acknowledgments

I want to express my gratitude to my family; my mother, sister and my friend, Rashed for their support and believe through my study journey. Also, I want to thank my aunts; Alia and Eman as well as uncle Ahmad for their support; especially aunt Alia for her regular phone calls. I am extremely grateful to all of you.

I would like to extend my deepest gratitude to my advisor; Dr. Daniel Foti. The completion of my thesis would not have been possible without the support and nurturing of Dr. Foti. Thank you for your support, time and for being patient and positive. Thank you very much.

I would also like to express my appreciation to my committee; Dr. John Hochstein and Dr. Ranganathan Gopalakrishnan. Special thanks to Dr. Gopalakrishnan for his time and support. Also, I want to thank Dr. Hochstein for providing the advice when it is needed and for the short talks from time to time.

Abstract

Wind turbine wakes are dominated by several energetic turbulent coherent structures that oscillate at specific Strouhal numbers. Implications on wind power harvesting of these dynamic, induced features require accurate unsteady modeling. Dynamic mode decomposition (DMD), a data-driven modal analysis, has demonstrated the ability to identify flow features based on specific frequencies. In this work, the selection of modes and data-driven DMD models pertaining to wakes with constant Strouhal number coherent structures are investigated using physically-informed criteria and sparse sampling. Both criteria are validated with a low Reynolds number flow behind a square cylinder. Next, the techniques are applied to data derived from the large-eddy simulation of a wind turbine wake. Modes related to tip vortices and hub vortex system are identified. Sparse identification shows remarkable ability to select the optimal modes for reduced-order modeling. Error becomes nearly independent of the number of modes when using fewer than 10% of the modes.

Contents

List of Figures

CHAPTER 1

Introduction

Renewable energy plays an important role in electricity production. For example, the United States plans to add 72 gigawatts (GW) of new wind and solar photovoltaic capacity between 2018 and 2021. It is expected that wind energy will have a more significant role in total capacity and account for 20% of the additional energy production (50 GW to 128 GW by 2021) (U.S. Energy Information Administration, 2019). Most of that electricity is expected to be generated by large wind farms, which consist of an array of wind turbines, which have diameter on the order of 100 m. High turbulence kinetic energy produced in the wake of wind turbines has a significant impact on the energy production, energy production variability, and wind turbine maintenance costs due to high dynamic loading. Understanding the fundamental features of turbulence towards reduced-order modeling can enable accurate energy production predictions for wind farms, which will increase the viability of wind energy.

A computationally expedient approach for modeling wind farms is to employ a theoretical model. Theoretical models, surveyed in Crespo et al. (1999) and Stevens and Meneveau (2017), for wind farms classified as either a bottom-up approach built on individual wind turbine wake structures (Jensen, 1983, Bastankhah and Porté-Agel, 2014, Lissaman, 1979) or the top-down approach based on the atmospheric boundary layer structure (Frandsen, 1992, Frandsen et al., 2006, Calaf et al., 2010). The former is based on jet mixing theory, is designed based on a single wind turbine, and referred to as kinematic models. In order to model a wind farm, superposition of the temporally averaged velocity deficit at the hub height of the wind turbine, treated as a passive scalar, is assumed (Lissaman, 1979). The superposition procedure can lead to nonphysical wake velocities as more wind turbines are included in the farm (Katic et al., 1986, Crespo et al., 1999). Another drawback is that the kinematic do not include effects from the atmospheric boundary layer. The latter top-down approach, often referred to as a distributed roughness model, is based an equilibrium between the wind turbine wakes and the atmospheric boundary layer. The distributed roughness model assumes the interaction is that of a fully-developed wind farm. The vertical velocity

profile is modeled based the present of two logarithmic layers, one below and one above the wind turbine in a temporally and horizontally-averaged streamwise velocity profile. The spacing between wind turbines is a free parameter that can be adjusted similar to kinematic models (Calaf et al., 2010, Yang et al., 2012). Both types of modeling approaches produce mean velocity distributions by assuming a steady-state conditions and captures mean power production.

A dynamic wake meandering model (Larsen et al., 2008, Madsen et al., 2010) considers downstream wake meandering phenomenon and stochastic turbulence but assumes a steady wake velocity deficit is transported as a passive scalar. The unsteadiness in the wake model is driven by assumptions based on the wake meandering phenomenon, which a large-scale oscillation of the wind turbine wake (Medici and Alfredsson, 2006, 2008). Wake meandering is a dominate far wake feature that is found to have a regular Strouhal number (Okulov et al., 2014), the non-dimensional frequency based on the diameter and hub height velocity. The dynamic wake meandering model considers that large eddies convecting in the atmospheric boundary layer displace the velocity deficit while downwind variations in the wake are assumed to be negligible due to Taylor's frozen hypothesis (Larsen et al., 2008). However, wake meandering is also affected by bluff-body vortex shedding (Foti et al., 2016, Yang and Sotiropoulos, 2019). Furthermore, the interactions between wind turbines in a wind farm are not fully understood and have complex dynamics that play an important role in power production and its variablility (Foti et al., 2019), which can lead to inaccuracies when employing theoretical models.

A complex system of helical vortices that dominates the flow behind the wind turbine. The system is comprised of N tip vortices for an N-bladed wind turbine and a center hub vortex (Joukowski, 1912). Tip vortices have been characterized by several experimental (Chamorro and Porté-Agel, 2009, Hu et al., 2012) and computational studies (Ivanell et al., 2009, Troldborg et al., 2007). These studies showed that the tip vortices convect downstream due to the relatively high-speed flow near the blade tip and eventually break down, a process which depends on many factors, such as the turbulence in the incoming flow, rotational speed, geometry of the turbine blade, and the interactions of helical vortices (Widnall, 1972). The center hub vortex has recently received more attention. Felli et al. (2011)

experimentally visualized the hub vortex of a propeller in a water tank and observed that it also undergoes instabilities and breaks down. Kang et al. (2014) showed that the hub vortex of a hydrokinetic turbine augments the far wake meandering. The hub vortex for a model wind turbine was also shown to impact wake meandering (Foti et al., 2016). The interaction of the hub vortex with the outer wake (the wake formed by the rotor blades) occurs several diameters down wind of the rotor and is a function of the operating condition of the wind turbine (Foti et al., 2018a). The unstable hub vortex oscillates at a frequency related to the rotation of the rotor (Iungo et al., 2013). While the Strouhal number of the tip vortices is directly related to the turbine rotor angular velocity, the hub vortex has been shown to have a regular Strouhal number of approximately 0.7 (Iungo et al., 2013, Viola et al., 2014, Foti et al., 2016). These coherent structure with two distinct frequency convect and breakdown into the onset of wake meandering in the far wake. The frequency of wake meandering has been measured both experimentally and computationally to be about $0.1 < \mathrm{St} < 0.3$ (Foti et al., 2016, 2018a,b, Okulov et al., 2014, Chamorro et al., 2013, Medici and Alfredsson, 2008).

With the rise of data from high-fidelity simulation and observation, data-driven approaches have been introduced to capture the complex spatio-temporal dynamics. In particular, modal decompositions, such as proper orthogonal decomposition (Holmes et al., 2012) and dynamic mode decomposition (Schmid, 2010) (DMD) provide an approach for identifying and modeling complex dynamics. Due to the presences of a few dominant frequencies in the wake of a wind turbines, DMD, where modes are based on specific frequencies, is particularly appealing. Furthermore, an efficient reduced-order model based on selection of certain DMD modes can be used to account for the dominant features in the flow field without over-simplification of the wake physics (Kutz et al., 2016). The selection of dominant modes remains a difficult task. In order to reduce arbitrary selection and provide a measure of optimality, sparse sensing, a data-driven technique that employs optimal locations based on compressive sampling (Manohar et al., 2018), is sought for DMD. Compressive sampling theory leverages low-dimensional sub-spaces induced by the data rather than directly measuring the high-dimensional signal (Donoho, 2006, Fowler, 2009, Baraniuk et al., 2010). In fluid dynamics, sparse sensing has been used to reconstruct flows from relatively few data

points (Bright et al., 2013), reduce dimensionality in Galerkin projection reduced-order models (Drmac and Gugercin, 2016), and enhance adaptive mesh refinement algorithms Foti et al. (2020). Complex wind turbine flows are characterized by coherent structures, which can be described on a low-dimensional manifold. Compressive sampling paired with dynamic mode decomposition has been shown to select sparse modes with optimal amplitudes (Jovanović et al., 2014). In this work, we will assess this behavior for wind turbine wakes to ascertain if a sparse selection of the modes correspond the dominant coherent structures in the wake.

DMD of the wake of wind turbine has recently been used to analyze the turbulence coherent structures present in the wake. The mutual induction of tip vortices was studied and low-fidelity vortex model was developed from the findings (Sarmast et al., 2014). Wake meandering, a large-scale oscillation of the wake, and unstable hub vortex were investigated in two different operating conditions of a model wind turbine (Foti et al., 2018a) with DMD. Because both wake meandering and the hub vortex are dominant coherent structures with periodic oscillations, the frequencies remain constant and can be easily isolated using DMD. The reconstruction of wake meandering amplitudes and wavelengths (Foti et al., 2016) with DMD was shown need relatively few DMD modes.

In this work, we use DMD to develop an efficient reduced-order model (ROM) for wind turbine wake that can capture the unsteady dynamics of wake meandering. We hypothesize that by selecting a few appropriate DMD modes, the flow field can be reconstructed accurately and can lead to predictions. It was shown that different levels of accuracy can be achieved by selecting different number of modes for the reduced order model (Debnath et al., 2017). Here, we develop a DMD-based framework for wind turbine wakes using data derived from large-eddy simulation (LES). First, The DMD are applied on a square cylinder for validation. After that, the DMD-based ROM will be developed for a wind turbine wake based on LES simulation. The intended outcome of the ROM will be extend the modelling to wind farms.

Need for further research

A major effort in wind turbine research involves the investigation of a model of the wakes behind the wind turbines. It is important to be able to understand and adequately model

the wake to be able to predict wind plant performance and optimize the turbine placement and controls. The complexity of the physics of wake is increased with the recent findings of the role of the unstable hub vortex (Kang et al., 2014, Iungo et al., 2013). This work seeks to capture the essential features in the wake. Wind turbine models do not take into account all the unsteady and dynamic effects of the wind turbine especially wake effects caused by the nacelle that could affect the intensity of far wake meandering. The inability of models to capture all the complex physics in the far wake can have significant implications for creating models for wind plant design and performance.

Research Objectives

The objectives of this research are to develop a data-driven modeling framework for a wind turbine wake. Below are specific objectives for this work:

1. Development, verification and validation of computational tools including dynamic mode decomposition and large-eddy simulation using a simplified flow over a square cylinder:
    - Compare the value of Strouhal number with the experimental values.
2. Establish flow characteristic and identify dominant features in a wind turbine wake using high-fidelity large-eddy simulation:
    - Develop high-fidelity large-eddy simulation for a flow behind the wind turbine.
    - Use DMD to capture the highest amplitudes.
    - Capture the frequencies that have these highest amplitudes.
3. Development a reduced-order model of a wind turbine wake based on dynamic mode decomposition:
    - Use the data of highest amplitudes and their frequencies to build a model that predicts the behavior of flow field behind the wind turbine.

The thesis is organized as follows:

- Chapter 2 reports the governing equations for three-dimensional, incompressible flow to perform large-eddy simulations for square cylinder and wind turbine applications, comprehensive explanation for mode decompositions, dynamic mode decomposition and sparsity-promoting DMD.
- Chapter 3 details a preliminary study of flow over a square cylinder.
- Chapter 4 provides details of the study of DMD and reduced order modeling of a wind turbine wake.
- Chapter 5 provides the summary of the results and conclusions for the thesis.

CHAPTER 2

Governing Equations and Numerical Methods

In this chapter, the governing equations for three-dimensional, incompressible flow will be presented, followed by brief explanation about mode decomposition techniques and comprehensive explanation about DMD and sparsity-promoting DMD. The numerical methods presented are developed for high-performance computing using a distributed memory scheme.

Large-eddy simulations

The LES is carried by solving the three dimensional, incompressible, filtered continuity and momentum conservation equations in three dimensional generalized curvilinear coordinates (Ge and Sotiropoulos, 2007) with a hybrid staggered/non-staggered grid formulation (Gilmanov and Sotiropoulos, 2005), which in curvilinear coordinates in compact tensor notation (repeated indices imply summation) are as follows ($i, j = 1, 2, 3$):

$$J\frac{\partial U^i}{\partial \xi^i} = 0, \tag{1}$$

$$\frac{1}{J}\frac{\partial U^i}{\partial t} = \frac{\xi_l^i}{J}\left(-\frac{\partial}{\partial \xi^j}(U^j u_l) + \frac{\mu}{\rho}\frac{\partial}{\partial \xi^j}\left(\frac{g^{jk}}{J}\frac{\partial u_l}{\partial \xi^k}\right) - \frac{1}{\rho}\frac{\partial}{\partial \xi^j}\left(\frac{\xi_l^j p}{J}\right) - \frac{1}{\rho}\frac{\partial \tau_{lj}}{\partial \xi^j}\right), \tag{2}$$

where $\xi_l^i = \partial \xi^i / \partial x_l$ are the transformation metrics, J is the Jacobian of the geometric transformation, u_i is the i^{th} component of the velocity vector in Cartesian coordinates, $U^i = (\xi_m^i / J) u_m$ is the contravariant volume flux, $g^{jk} = \xi_l^j \xi_l^k$ are the components of the contravariant metric tensor, ρ is the density, μ is the dynamic viscosity, p is the pressure, and τ_{ij} represents the anisotropic part of the subgrid-scale stress tensor. The closure for τ_{ij} is provided by a dynamic Smagorinsky model (Smagorinsky, 1963) developed by (Germano et al., 1991).

$$\tau_{ij} - \frac{1}{3}\tau_{kk}\delta_{ij} = -2\mu_t \widetilde{S}_{ij}, \tag{3}$$

where the $\tilde{.}$ denotes the grid filtering operation, and $\widetilde{S}_{ij}$ is the filtered strain-rate tensor. The eddy viscosity μ_t is given by

$$\mu_t = \rho C_s \Delta^2 |\tilde{S}|, \tag{4}$$

where C_s is the dynamically calculated Smagorinsky constant (Germano et al., 1991), Δ is the filter size taken as the cubic root of the cell volume, and $|\tilde{S}| = (2\widetilde{S}_{ij}\,\widetilde{S}_{ij})^{\frac{1}{2}}$. A wall model is used to reconstruct boundary conditions at the immersed boundary nodes (Kang et al., 2012). The governing equations are discretized with three-point central finite differencing on a hybrid staggered/non-staggered grid and integrating in time using an efficient fractional step method (Kang et al., 2012, 2014).

Mode Decomposition Techniques

In this part, we will discus the two mode decomposition techniques that have a strong direct relation with DMD:

1. Singular value decomposition (SVD).

2. Proper orthogonal decomposition (POD).

Singular Value Decomposition

First we start with SVD; since it is the first step in the POD and DMD algorithm. The importance of SVD is that it is considered as a dimensional data reduction tool, so with SVD, we can build low-dimensional models that present the original high-dimensional model.
The SVD of a matrix X is:

$$X = U\Sigma V^*, \tag{5}$$

Or:

$$\mathrm{X}= \underbrace{\begin{bmatrix} | & | & ... & | \\ u_1 & u_2 & ... & u_m \\ | & | & ... & | \end{bmatrix}}_{U\in\mathcal{R}^{n\times m}} \underbrace{\begin{bmatrix} \sigma_1 & & \\ & \ddots & \\ & & \sigma_m \end{bmatrix}}_{\Sigma\in\mathcal{R}^{m\times m}} \underbrace{\begin{bmatrix} - & v_1 & - \\ - & v_2 & - \\ \vdots & \vdots & \vdots \\ - & v_m & - \end{bmatrix}^*}_{V\in\mathcal{R}^{m\times m}}$$

Where * denotes the conjugate transpose, and the matrix $U \in \mathcal{R}^{n \times m}$ are the left singular vectors and has the same size as matrix X, $\Sigma \in \mathcal{R}^{m \times m}$ are the singular values, and $V \in \mathcal{R}^{m \times m}$ are the right singular vectors.

Also, the columns of the matrix U are orthonormal vectors. U and V are unitary which means $UU^* = U^*U = I$, and $VV^* = V^*V = I$.

Σ is a diagonal matrix, and its elements are real positive numbers and they are hierarchically arranged so; $\sigma_1 > \sigma_2 > ... > \sigma_m$. The important fact about SVD is that the space and time correlations between U and V. So, U has the spatial modes or POD modes in its vectors, while V describes the evolution of these modes in time.

The procedure to find Σ, V and U is by multiply (5) by X^T to get:

$$\begin{aligned} X^T X &= (U\Sigma V^*)^T (U\Sigma V^*) \\ &= V\Sigma U^* U\Sigma V^* \\ &= V\Sigma^2 V^*, \end{aligned}$$

Then multiply the above equation by V:

$$\begin{aligned} X^T XV &= V\Sigma^2 V^* V \\ X^T XV &= V\Sigma^2, \end{aligned}$$

Assuming that $X^T X = G$ and $\Sigma^2 = B$ you get the eigenvalue problem, then solve for V and B:

$$GV = BV \tag{6}$$

After computing V and Σ, flowing the same approach, it is possible to compute U or POD modes:

$$\begin{aligned} XX^T &= (U\Sigma V^*)(U\Sigma V^*)^T \\ &= U\Sigma V^* V\Sigma U^* \\ &= U\Sigma^2 U^*, \end{aligned}$$

Then multiply the above equation by U:

$$XX^TU = U\Sigma^2U^*U$$
$$XX^TU = U\Sigma^2,$$

Assuming that $XX^T = T$ but $\Sigma^2 = B$ you get the eigenvalue problem, then solve for V and B:

$$TU = BU \tag{7}$$

We have T and B, so we can find U. Or, we can reconstruct U form matrix X after computing V and Σ from (6) by:

$$U = XV\Sigma^{-1} \tag{8}$$

Dynamic Mode Decomposition

Snapshot-based method

Snapshot-based method is used to collect the data of velocity measurements of the flow field, the collected data is organized into columns (Kutz et al., 2016):

$$x(c, t_i) = \begin{bmatrix} x(c_{1,1}, t_i) & x(c_{1,2}, t_i) & ... & x(c_{1,y}, t_i) \\ x(c_{2,1}, t_i) & x(c_{2,2}, t_i) & ... & x(c_{2,y}, t_i) \\ | & | & | & | \\ x(c_{z,1}, t_i) & x(c_{1,2}, t_i) & ... & x(c_{z,y}, t_i) \end{bmatrix},$$

$$\mathrm{x}_i = \begin{bmatrix} x(c_{1,1}, t_i) \\ x(c_{1,2}, t_i) \\ | \\ x(c_{2,1}, t_i) \\ | \\ (c_{z,y}, t_i) \end{bmatrix},$$

where, x is the flow variable (velocity measurements); so x_i is the snapshot at time t_i, where i represents the ith time step. After that, we organize these columns of snapshots into matrix X and matrix X' (Kutz et al., 2016):

$$X = \begin{bmatrix} | & | & ... & | \\ x_1 & x_2 & ... & x_m \\ | & | & ... & | \end{bmatrix}, X^{'} = \begin{bmatrix} | & | & ... & | \\ x_2 & x_3 & ... & x_{m+1} \\ | & | & ... & | \end{bmatrix}.$$

DMD Algorithm

DMD is a promising technique used to capture the dominant spatiotemporal coherent structures that govern a flow fluid. The DMD method decomposes the flow variable that is collected from snapshots of measurements or simulations into the sum of its spatio-temporal components (Kutz et al., 2016).

$$X = \begin{bmatrix} | & | & ... & | \\ x_1 & x_2 & ... & x_m \\ | & | & ... & | \end{bmatrix}, X^{'} = \begin{bmatrix} | & | & ... & | \\ x_2 & x_3 & ... & x_{m+1} \\ | & | & ... & | \end{bmatrix}$$

where, $X, X' \in \mathcal{R}^{n \times m}$, where n is the number of degrees of freedom in a snapshot and m is the number of snapshots. Each snapshot is uniformly sampled in time separated by Δt. DMD is an operator-theoretic spectral analysis related the linear mapping A associated with the full non-linear system (Rowley et al., 2009). The linear mapping relates the vector-valued observable x between two consecutive snapshots as follows:

$$X^{'} = AX \tag{9}$$

In this analysis, we used the DMD algorithm derived in Ref. (Schmid, 2010), which uses singular value decomposition regularization.

The SVD of X is computed as:

$$X = U\Sigma V^{*} \tag{10}$$

where * denotes the conjugate transpose, $U \in \mathcal{R}^{n \times r}$ are the left singular vectors, $\Sigma \in \mathcal{R}^{r \times r}$ are the singular values, and $V \in \mathcal{R}^{m \times r}$ are the right singular vectors. The rank r is the reduced SVD. The snapshot matrix A may be obtained by using the pseudoinverse of X:

$$A = X^{'} V \Sigma^{-1} U^{*} \tag{11}$$

However introduced in Ref. (Schmid, 2010), a reduced linear operator $\tilde{A} \in \mathcal{R}^{r \times r}$ can more efficiently obtained by projecting A with the orthogonal left singular vectors as follows:

$$\tilde{A} = U^* A U = U^* X^{'} V \Sigma^{-1} \tag{12}$$

The matrix $\tilde{A}$ is the reduced mapping of the dynamical system.
Spectral information of the $\tilde{A}$, which has been shown to be the same at A are obtained through an eigendecomposition as follows:

$$\tilde{A} W = W \Lambda \tag{13}$$

where, columns of W are eigenvectors and Λ is a diagonal matrix containing the corresponding eigenvalues λ_i. The eigenvalues λ_r are complex conjugates which all lie on the complex unit circle, $|\lambda_r| = 1$. To obtain the more familiar complex frequency $\imath\omega_r = \log(\lambda_r)/\Delta t$. The real part is the temporal frequency, and the imaginary part is an exponential growth rate of the dynamic mode. The spatial dynamic modes Φ are recovered with

$$\Phi = X^{'} V \Sigma^{-1} W \tag{14}$$

The reduced system x_r using r modes can be constructed with the following linear summation:

$$x_r = \Phi \exp(\Omega t) b \tag{15}$$

where b is the amplitude vector. The amplitudes b are computed based on the initial snapshot (Kutz et al., 2016):

$$b = \Phi^{\dagger} x_1 \tag{16}$$

where, $\dagger$ is the Moore–Penrose pseudoinverse. And b is the best-fit solution that has the least-squares sense (Kutz et al., 2016). However, in high dimensional cases, we first calculate the amplitudes then we construct the reduced system.

Sparsity-promoting DMD

With this technique, we are trying to compute the optimal amplitudes of modes that are used in the reduced order models (ROMs) using sparse sensing (Jovanović et al., 2014). These amplitudes are the amplitudes that capture the most important dynamics of the flow

field. The algorithm used here has been developed by (Jovanović et al., 2014). Also, the sparsity- DMD will be introduced as it is presented in Ref. (Jovanović et al., 2014). So, first, the optimization problem is presented in the next subsubsection, then the sparsity will be introduced followed by the steps of solving the optimization problem using the Alternating Direct Method of Multiplies (ADMM).

Optimal amplitudes of DMD modes

It is difficult to select the appropriate number of DMD modes for a ROM using Eqn. (16). Also, the optimal amplitudes of the DMD modes computed by Eqn. (16) are based on the first velocity snapshot. Sparsity- DMD computes the optimal amplitudes of the DMD modes, $b = [b_1, \ldots, b_r]^T$ using information from all snapshots and enables us to select the number of modes that will be used to build the ROM. After computing the SVD of the snapshot matrix X, and matrix $\tilde{A}$ and using V_{and} matrix to present the time evolution of the flow field, the flow variable can be presented as:

$$x_r = \sum_{i=1}^{r} \phi_i \lambda_i^t b_i, \quad t \in \{0, ..., N-1\} \tag{17}$$

where again, b_i is an element in vector b and it represents the amplitude of the ith DMD mode computed in Φ. So, Eqn. (17) is written as follows:

$$\underbrace{\begin{bmatrix} x_0, x_1, ..., x_{N-1} \end{bmatrix}}_{x_0} = \underbrace{\begin{bmatrix} \phi_0, \phi_1, ..., \phi_r \end{bmatrix}}_{\Phi 0} \underbrace{\begin{bmatrix} b_1 & & & \\ & b_2 & & \\ & & \ddots & \\ & & & b_r \end{bmatrix}}_{D_b \;=\; diag(b)} \underbrace{\begin{bmatrix} 1 & \lambda_1 & \ldots & \lambda_1^{N-1} \\ 1 & \lambda_2 & \ldots & \lambda_2^{N-1} \\ \vdots & \vdots & \ddots & \vdots \\ 1 & \lambda_r & \ldots & \lambda_r^{N-1} \end{bmatrix}}_{V_{and}}$$

where again, λ_r are the eigenvalues of $\tilde{A}$. We solve for b by solving this optimization problem (Jovanović et al., 2014):

$$\underset{b}{\text{minimize}} \quad J(b) = \|X - \Phi D_b V_{and}\|_F^2$$

Function $J(b)$ has the sense of least square between the actual flow field and the ROM. The goal is to find the vector b such that, $J(b)$ has the minimum value. Jovanović et al. (2014) shows that the objective function $J(b)$ can be represented as :

$$J(b) = b^* P b - q^* b - b^* q + s \tag{18}$$

where, $P = WW^* \cdot (\overline{V_{and} V_{and}^*})$, $q = \overline{diag(V_{and} V \Sigma^* W)}$, s =trace(ΣV^*). And again, * denotes the conjugate transpose, while the complex conjugate represented by the overline. The diag of a vector produces a diagonal matrix of the components of that vector, while the diag of a matrix is a vector contains the components of the main diagonal of that matrix. The $\cdot$ is the elementwise multiplication. And finally, $b_{dmd} = P^{-1} q = (WW^* \cdot (\overline{V_{and} V_{and}^*}))^{-1} \overline{diag(V_{and} V \Sigma^* W)}$ (Jovanović et al., 2014).

Sparse solution

The sparse solution is induced by adding the cardinality of vector b; $card(b)$, to the original optimization problem (Jovanović et al., 2014):

$$\underset{b}{\text{minimize}} \quad J(b) + \gamma card(b) \tag{19}$$

For high dimensional problem like fluid mechanics, the $card(b)$ is replaced by the l_1-norm,

$$\underset{b}{\text{minimize}} \quad J(b) + \gamma \sum_{i=1}^{r} |b_i| \tag{20}$$

γ is a positive parameter that controls the sparse sensing of the vector b. So, the sparsity of the DMD modes is controlled by γ.

After introducing the sparsity, b is computed by solving Eqn. (21):

$$\begin{aligned} &\underset{b}{\text{minimize}} \quad J(b) \\ &\text{subject to} \quad E^T b = 0 \end{aligned} \tag{21}$$

where, matrix $E \in \mathcal{R}^{r \times e}$, and e is the number of zero elements in b. The columns of E are unit vectors such that the non-zero elements are corresponding to zero components of b (Jovanović et al., 2014). The algorithm to solve Eqn. (21) is provided in Appendix B (Jovanović et al., 2014).

Alternating direction method of multipliers

The Alternating direction method of multipliers for solving Eqn. (20) consists of two steps as it is shown in (Jovanović et al., 2014).

Step 1: Decouple g from J using a new variable β:

$$\begin{aligned} \underset{b,\beta}{\text{minimize}} \quad & J(b) + \gamma g(\beta) \\ \text{subject to} \quad & b - \beta = 0 \end{aligned} \tag{22}$$

where, $g(b) = \sum_{i=1}^{r} |b_i|$.

Step 2: Use the augmented Lagrangian:

$$\mathcal{L}_\rho(\mathrm{b}, \beta, \mu) = J(b) + \gamma g(\beta) + \frac{1}{2}(\mu^*(b - \beta) + (b - \beta)^*\mu + \rho\|b - \beta\|_2^2$$

Where, μ is the Lagrange multipliers vector , ρ is a positive parameter, and for our case, $\rho = 1$. The three steps of ADMM algorithm are; b-minimization step, β-minimization step, and μ update step:

$$b^{k+1} = \underset{b}{\arg} \quad \min \quad \mathcal{L}_\rho(b, \beta^k, \mu^{k+1}) \tag{23}$$

$$\beta^{k+1} = \underset{\beta}{\arg} \quad \min \quad \mathcal{L}_\rho(b^{k+1}, \beta, \mu^k) \tag{24}$$

$$\mu^{k+1} = \mu + \rho(b^{k+1} - \beta^{k+1}) \tag{25}$$

Appendix A shows the algorithm of solving Eqn. (20) (Jovanović et al., 2014). To summarize the approach, the sparse solution is introduced by the l_1-norm in Eqn. (20), then Eqn. (21) solves for the vector b. By using sparsity- DMD, we can find or compute the most important modes that will be used to build the ROM.

CHAPTER 3

Low Reynolds Number Verification and Validation Case

In a preliminary study, the flow around a square cylinder with Re. $= U_\infty D/\nu = 175$, where $U_\infty = 1$, is the incoming velocity, $D = 1$ is the diameter, and ν is the kinematic viscosity. The flow is simulated within a quasi-two-dimensional computational domain in the vertical and streamwise directions $(L_y \times L_z) = (12D \times 18D)$, with periodic boundaries in the spanwise x-direction. A negligible thickness in the L_x direction is included because the CURVIB method is implemented in three dimensions. The computational domain is discretized with $(N_x \times N_y \times N_z) = (6 \times 201 \times 351)$ grid points with uniform spacing within D of the square cylinder and stretching in the vertical and streamwise directions towards all of the boundaries. Slip-wall boundary conditions are used on the upper and lower walls with an impose incoming volumetric flux in the inlet boundary and a convection outflow.

The simulation is run until the flow has converged and has become statistical steady. Then, $m = 2000$ instantaneous snapshots of the three velocity components are obtained with a uniform sampling of $\Delta t = 0.02$, and use for the DMD algorithm.

Dynamic mode decomposition-based reduced order model

In this section, DMD is employed to create a reduced-order model (ROM) of the flow around the square cylinder. The ROM is developed based on both modes amplitudes and eigenvalues. In order to accomplish this task, the dynamic modes and their associated eigenvalues are assessed. Eigenvalues that fall inside the unit circle are strongly damped and their effects are dissipated (Schmid, 2010, Jovanović et al., 2014). The modes that are associated with these are not considered.

The first step of developing the ROM is to pick the modes that have the highest amplitudes that are also associated with undamped eigenvalues. Using this criteria the 2000 modes are reduced to 975 modes. Figure 1 shows the relative amplitudes and frequencies of some select modes. These 15 modes have the highest amplitudes that are associated with relatively undamped eigenvalues. Two frequencies obtained from DMD based on the non-dimensional Strouhal number St $= fD/U_\infty$ are St $= 0.159$ and and its harmonic multiple

0.318. These frequencies are consistent with the periodic von-Kármán vortex shedding and have been captured in previous experimental studies and simulations (Sharma and Eswaran, 2004, Sohankar et al., 1999).

Although, these two frequencies are not associated with the highest amplitude, they are still in the highest 0.75% amplitudes and their eigenvalues lie on the unit circle, which indicates that the effects of these modes will not dissipate with time.

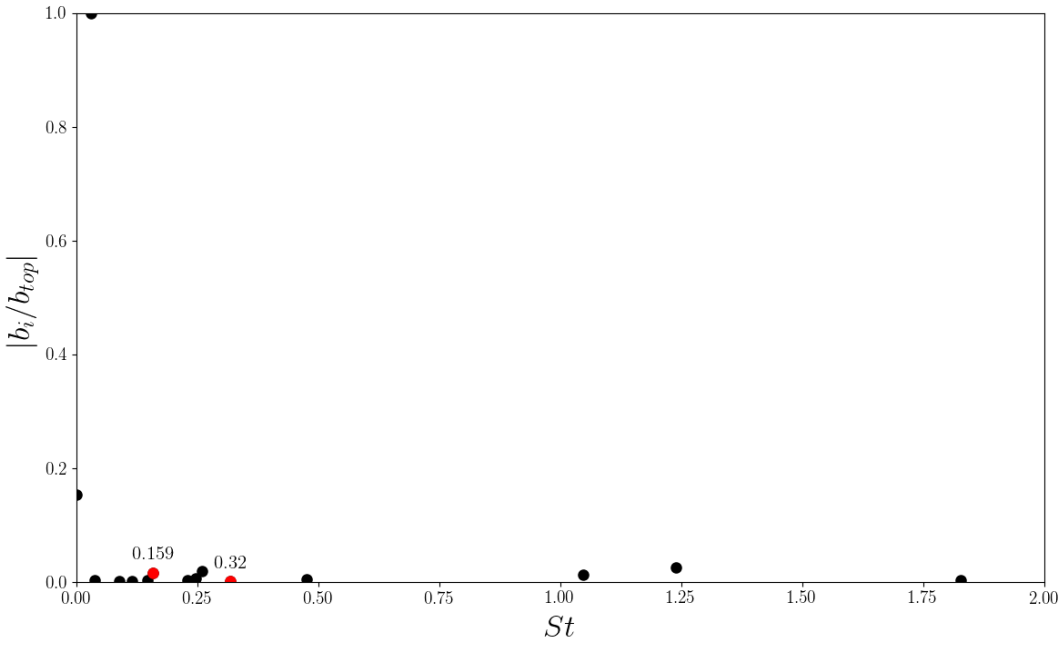

Figure 1: Relative amplitudes of most important 15 modes with their corresponding Strouhal number St. The red makers are the eigenvalues for frequencies St = 0.159 and St = 0.318.

The main goal of DMD is to develop the ROM based on the most important modes and their frequencies. The power spectral density (PSD) of velocity time series at particular locations in the flow is used to identify frequencies associated with high energy contributions. The PSD shows the energy distribution in the flow field.

Figure 2 shows the PSD as a function of Strouhal number at two locations downstream after the square cylinder along the centerline: $x/D = 1$ and $x/D = 3$. Figure 2 indicated that there are two frequencies close to St = 0.159 and 0.318 associated with high energy modes.

These frequencies agrees with those identified with DMD and prior investigations (Sharma and Eswaran, 2004, Sohankar et al., 1999).

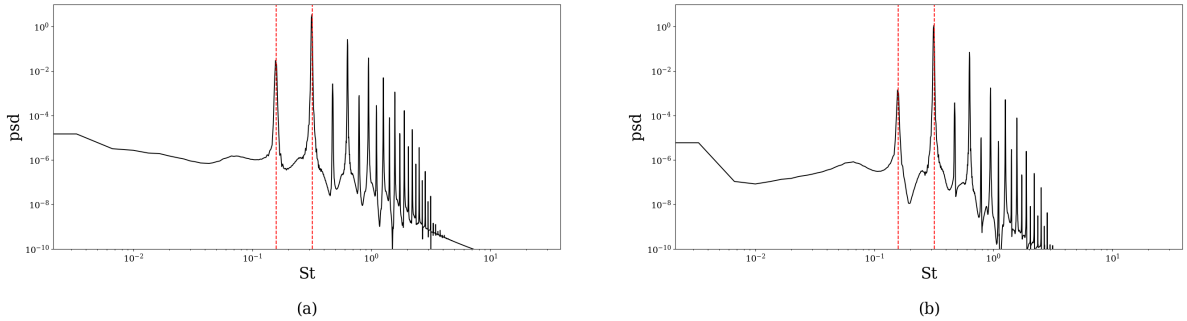

Figure 2: PSD as a function of St for (a) $x/D = 1$ (b) $x/D = 3$ downwind the cylinder.

The eigenvalues of the 2000 DMD modes on the real-complex plane are show in Fig. 3. The eigenvalues associated with the top 15 amplitudes are identified on the figure.

Figure 4 shows the dynamic models of four selected modes of the ROM. Figure 4(a) shows the mode with frequency St = 0.03, which is the highest amplitude. Figure 4(b) shows the mode associated with the time averaged flow and a frequency, St = 0, Figure 4(c) and 4(d) show the two modes that are associated with the vortex shedding, St = 0.159 and St = 0.318, respectively.

An initial case of a ROM with 975 modes is built based on Eqn. (15). Figure 5(a) and (b) show contours of the streamwise velocity of the simulation and the DMD-based ROM of the undamped 975 modes at the initial time, respectively. This suggests that the ROM can recover the many of the conditions. However, further work and insights are necessary to ascertain a fewer number of modes that can be used to accurately reconstruct the flow field.

Sparsity-promoting DMD-based reduced order model

The main goal of sparsity-promoting DMD is to reconstruct the flow field with less number of modes R that are used in the ROM to represent a given field.

Different ROMs are created with different R (12, 42 and 1879) to present the flow fields. The relation between R and the quality of our approximation is studied. Quantitative

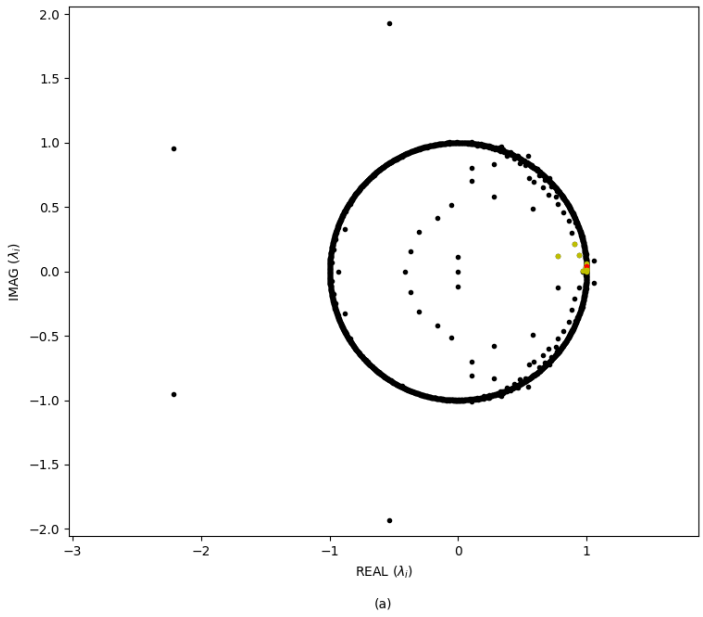

Figure 3: (a) Eigenvalues for the all 2000 modes and their location relative to unit circle and (b) eigenvalues that are associated with the selected 15 modes. Eigenvalues that are associated with the selected 15 modes in color: red are the eigenvalues associated with the vortex shedding with frequencies; St = 0.159 and its integer multiple frequency St = 0.32, and yellow are the other selected 13 modes with the high amplitudes.

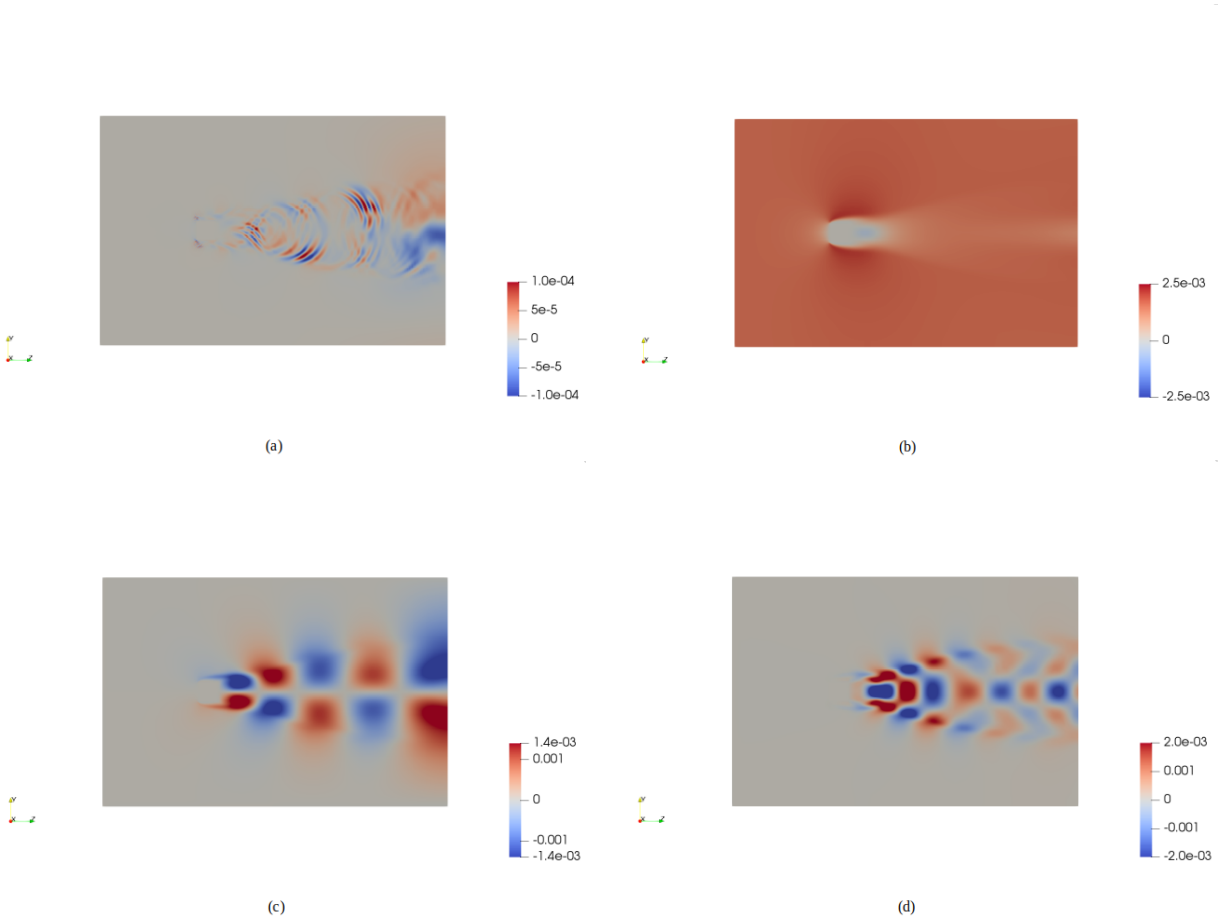

Figure 4: Contours of dynamic modes of the flow over a square cylinder for some selected modes: (a) St = 0.03, (b) St = 0, (c) St = 0.159, and (d) St = 0.318.

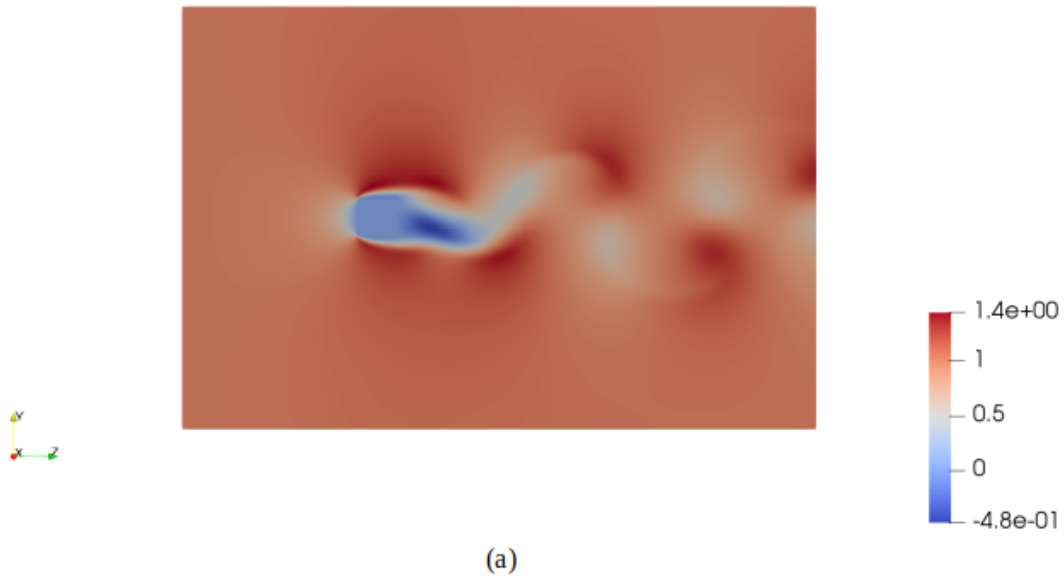

(a)

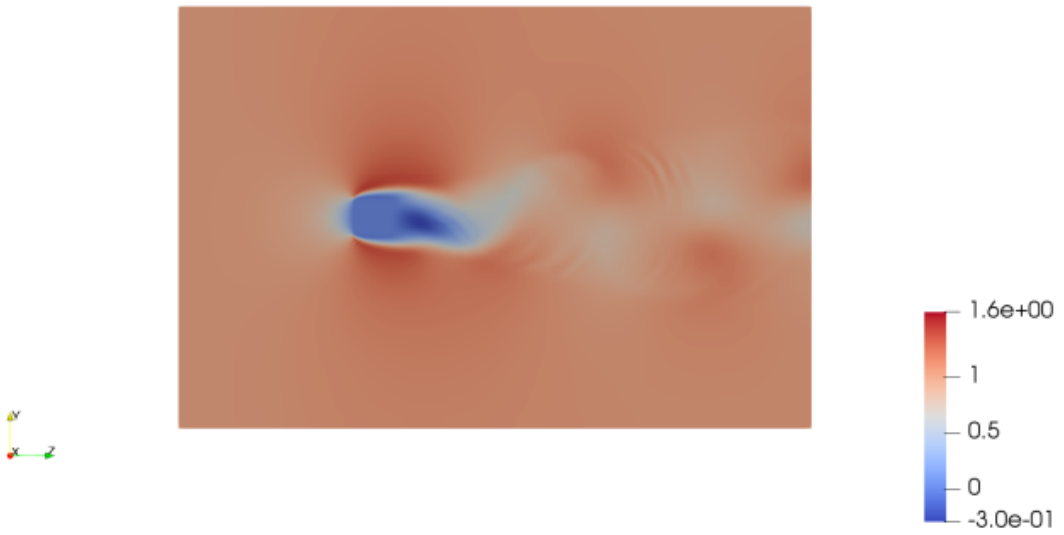

(b)

Figure 5: Contours of initial streamwise velocity from (a) the simulation and (b) the DMD-based ROM.

Table 1: Number of modes R and $\log_{10}(\gamma)$ value for each ROM.

$\log_{10}(\gamma)$	Number of Modes (R)
5	12
4	42
1.2	1879

standards are used to test the ROMs: the performance parameter ($\%loss$) and reconstruction error RE. The performance parameter is given by

$$\%\text{loss} = 100\frac{\|X - \Phi D_\alpha V_{and}\|_F}{\|X\|_F}.$$

The performance parameters ($\%loss$) is the residual $\|X - \Phi D_\alpha V_{and}\|_F$ between the actual flow field and the ROM, normalized by $\|X\|_F$, while the reconstruction error RE is calculated by the following:

$$\text{RE} = \frac{\|X_i - X_{ROM,i}\|}{\|X_i\|},$$

where X_i is the column of the original matrix X at time i, And $X_{ROM,i}$ is the column of the reduced order model X_{ROM} at that time. It is worth note to say that, each column of both; X_i and $X_{ROM,i}$ represents the velocity at that time. Each ROM is related to certain γ value as shown in Table 1.

Figure 6(a) shows the relation between γ and the $\%loss$, while Figure 6(b) shows the general relation between γ and R of the ROM. From Figure 6(b), we see that small γ values are associated with big number of modes that are used in the ROM which leads to less values of $\%loss$ as shown in Fig. 6(a) and Table 1. As γ increases, we promote the sparse solution by using less number of non-zero modes in the ROM.

We search for the frequencies that have the highest amplitudes. Figure 7 shows the relative amplitudes and frequencies of some selected modes. From the this figure, we see that St = 0.15 has the highest amplitude in the three different ROMs. Frequencies St = 0.15 and St = 0.32 are colored in blue. These frequencies correspond to St = 0.159 and St = 0.318

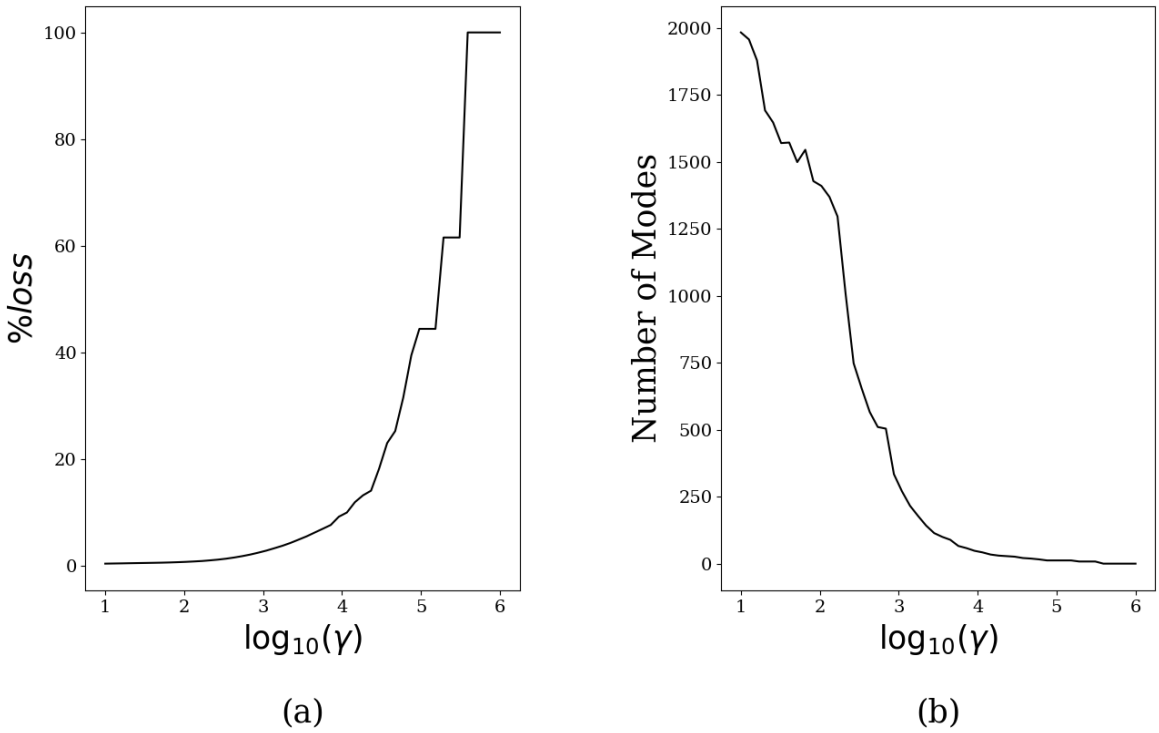

Figure 6: (a) The relation between γ and the $\%loss$, (b) the general relation between γ and the number of modes R of the ROM.

of the vortex shedding. This suggests that the sparsity-promoting DMD is able to identify the optimal modes that has the most dominant effects on the flow and eliminates the less important ones. The first ROM in Figure 7(a) shows the most dominant modes while the second ROM in Figure 7(b) contain the most 42 modes. Final Figure 7(c) shows the amplitude when selecting 1879 modes.

Figure 8 shows the eigenvalues for the all 2000 modes calculated by the sparsity-promoting DMD and their location relative to unit circle. Eigenvalues that are associated with the selected ROM modes are mauve ones and the blue ones are the eigenvalues of St = 0.15 and St = 0.32. Figure 8 shows that both St = 0.15 and St = 0.32 are undamped.

The reconstruction error, RE, is used to test the accuracy of ROM with evolution of time. Figure 9 is a plot of the RE values for the three ROMs. t is the time interval for which $t = [0, K]$ and $T = 1/0.159$ where St = 0.159 is the frequency of the periodic von-Kármán vortex shedding. The figure shows an acceptable value of RE with the maximum value less

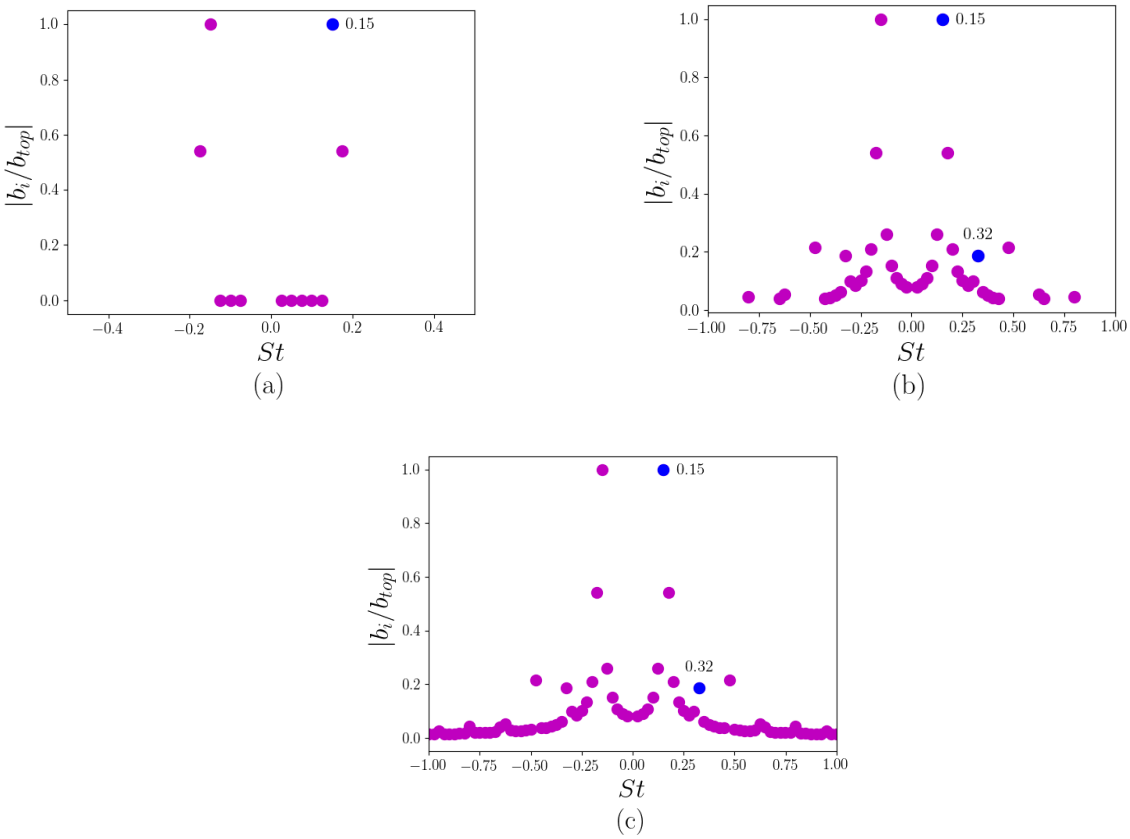

Figure 7: Relative amplitudes of three ROM(s) with the associated frequencies.(a) 12 modes, (b) 42 modes, (c) 1879 modes. The blue markers are the eigenvalues for frequencies St = 0.15 and St = 0.32.

that 30% in the prediction region. The more number of modes used in the ROM the lower RE, which is expected and also agrees with the $\%loss$ results.

It is also worth noting that we are trying to find a model that represents the flow field with optimal number of modes R such that acceptable values of RE are achieved. Finally, we can say that successful models have been built using 12 and 42 modes, which is less than the ROM of DMD.

Figure 10 shows the general trend between average value of reconstruction error RE_{avg} for different 8 ROMs with R, as the number of ROM modes increase the reconstruction error decreases which is expected.

To complete the picture, the streamwise velocity of the actual field and the three ROMs

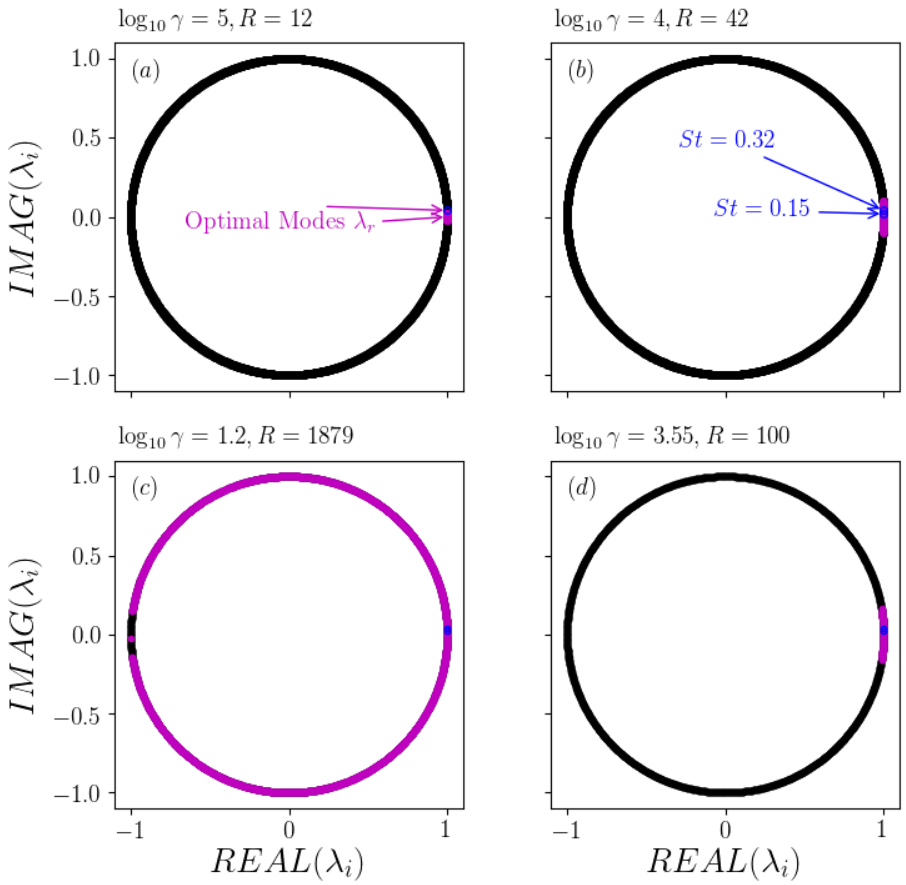

Figure 8: (a) Eigenvalues that are associated with the 12 modes ROM. (b) and (c) eigenvalues that are associated with the ROM of 42 and 1879 modes, respectively. (d) Eigenvalues associated with the ROM of 100 modes.

at different times are shown in Figs. 11 to 13. These figures give us a qualitative view about the ability of ROMs to represent the actual flow field.

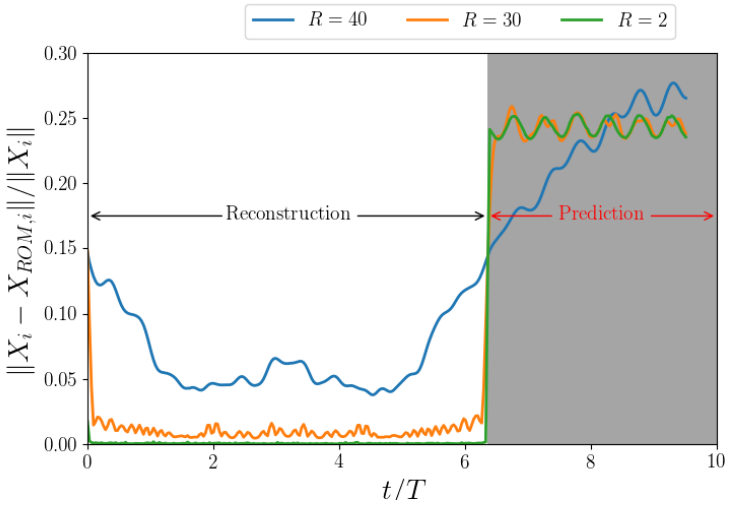

Figure 9: Reconstruction Error RE for the four ROMs.

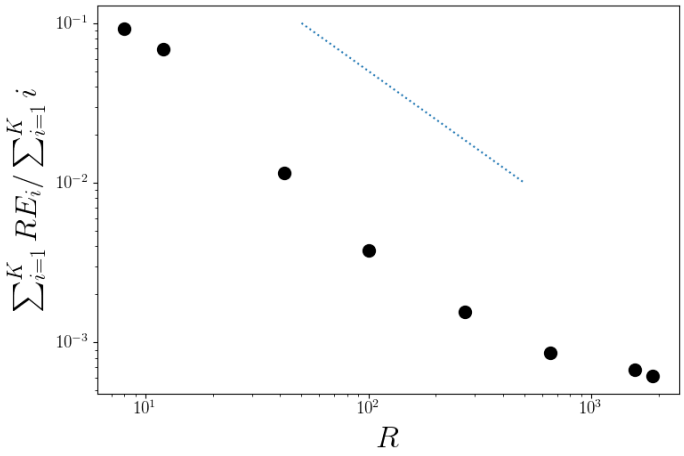

Figure 10: Average Value of Reconstruction Error RE_{avg} and the Number of ROM Modes R.

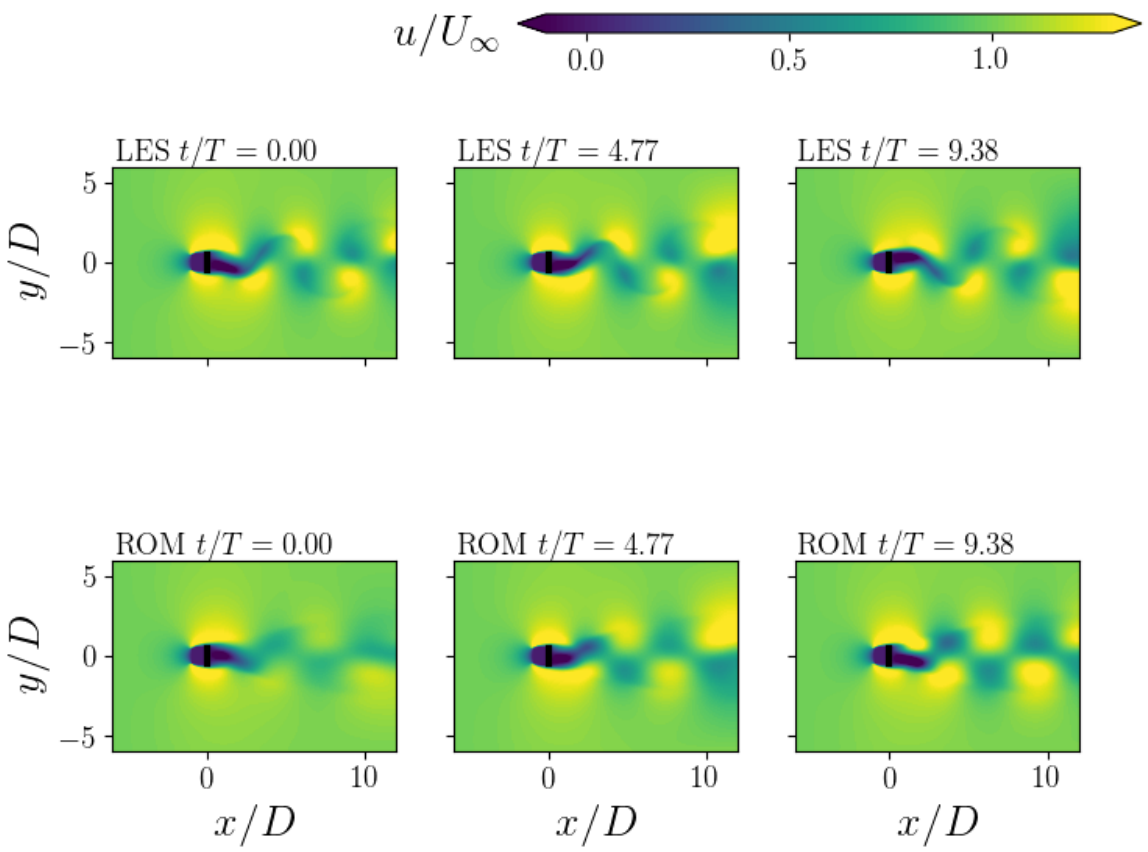

Figure 11: Contour of streamwise velocity of the wake for the actual flow and the reconstruction wake with 12 modes at different times. The top plot is the streamwise velocity of the actual flow, while the bottom is the streamwise velocity of the ROM.

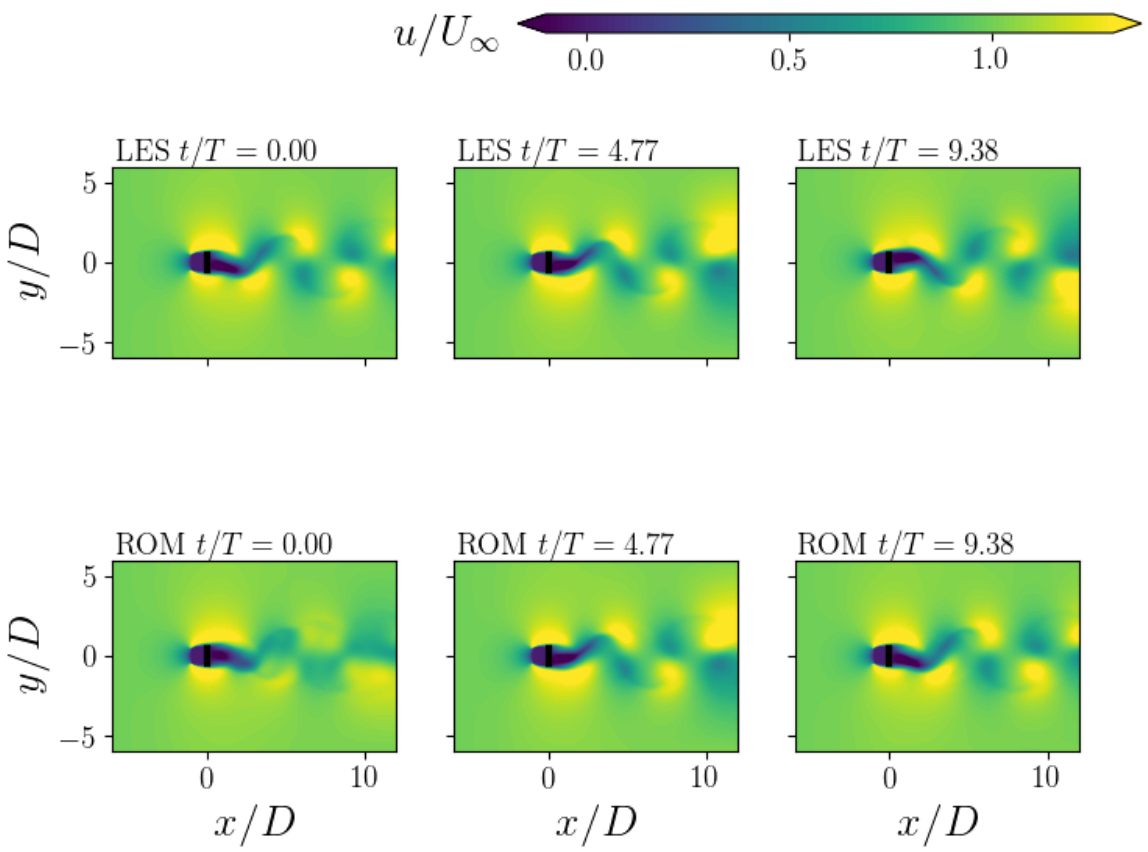

Figure 12: Contour of streamwise velocity of the wake for the actual flow and the reconstruction wake with 42 modes at different times. The top plot is the streamwise velocity of the actual flow, while the bottom is the streamwise velocity of the ROM.

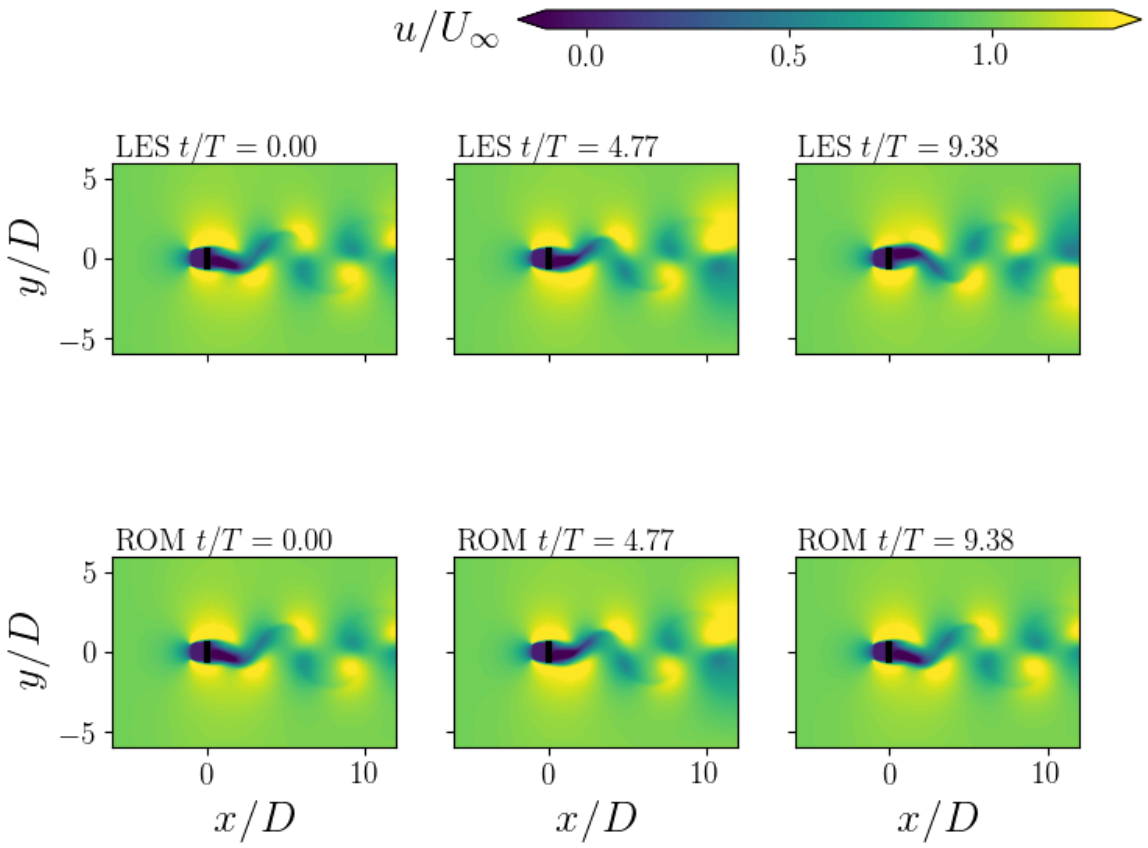

Figure 13: Contour of streamwise velocity of the wake for the actual flow and the reconstruction wake with 1879 modes at different times. The top plot is the streamwise velocity of the actual flow, while the bottom is the streamwise velocity of the ROM.

CHAPTER 4

Wind Turbine

In order to validate the framework for LES of a wind turbines, we begin by simulating a single wind turbine in a domain far from wall boundaries with a uniform velocity incoming wind around the rotor. In particular, we choose the rotor to resemble the Clipper Liberty C96 2.5 MW turbine deployed at the University of Minnesota Eolos Wind Energy Research Field Station in Rosemount, MN, USA (Yang et al., 2016, Foti et al., 2018b). The tip-speed ratio, $\lambda = \omega R/U_\infty = 8.0$, where ω is the angular velocity, R is the turbine radius and U_∞ is the hub height velocity, and the diameter D and U_∞ are normalized such that the Reynolds number $\mathrm{Re} = U_\infty D/\nu$, is based on the kinematic viscosity $\nu = 2 \times 10^{-5}$ m^2/s.

The computational domain is $(L_x \times L_y \times L_z) = (5D \times 4D \times 4D)$ discretized in a Cartesian stretch grid $(N_x \times N_y \times N_z) = (336 \times 251 \times 251)$ where a uniform grid with space of $D/50$ is located in a $2D$ cubic box around the turbine blades. With this discretization, we employ LES for turbulence modeling. Instead of using the curvilinear immersed boundary method to describe the movement of the blades, an actuator line method (Sorensen and Shen, 2002) as implemented in the Virtual Wind Simulator (Yang et al., 2015). The DMD was only performed on a subset of the entire computational domain. A uniform incoming velocity is chosen as a first step for DMD-based ROM. The tip vortices are well defined with this discretization. This work will involve using snapshots to decompose the flow field using DMD in order to study its behavior to implement with the DMD-based ROM.

We investigate the spatial distribution of the mean flow field. Figure 14(a) shows the mean streamwise of the flow field U/U_∞. Figure 14(a) shows as expected reduction in the velocity after the interaction between the incoming flow and the wind turbine rotor. Figure 14(b) shows turbulence kinetic energy k/U_∞ (TKE), this figure shows that, the intense turbulence regions start directly after the rotor hub. The interaction of the hub vortex with the outer wake (the wake formed by the rotor blades) occurs about 2 diameters down wind of the rotor is observed. Near this intersection, there is a marked increase in TKE. Figure 14(c) shows streamwise-vertical Reynolds shear stress $\overline{u'v'}/U_\infty$, this figure shows that vertical

Reynolds shear stress is high near the hub due to the high rotation in that region. It is clear form Figure 14(d) that the mean spanwise vorticity $\omega_z D/U_\infty$ is higher along the tip and hub level and that is due to the existence of hub and tip vortices.

Dynamic mode decomposition-based reduced order model

Before the applying the DMD to analyze the flow of the wind turbine, a parametric study was done to test the effect of changing the matrix size on the $Residual = \|X^{'} - XA\|/\|X^{'}\|\|A\|$, where X and $X^{'}$ are the two snapshot matrices, and A is the linear operator. The results of this study shows the Residual are converging with increasing the snapshot matrix size, as it is shown in Fig. 15.

As a first step, the PSD analysis of some points of the flow has been used to show the energy distribution of the flow field. PSD gives us information about the frequencies that have the highest energy. Figure 16 is PSD plot of some locations of the flow field. Figure 16 shows that St = 7.62 is one of the frequencies that have highest energy for the all points. This value is same as blade-passing frequency $St_{BPf} = 3 \times f_r = 7.6$ that is related to the tip vortices (Iungo et al., 2013). The rotor frequency $St_{rotor} = 2.54$.

The DMD is applied to a matrix of size $m = 400$ instantaneous snapshots with a uniform sampling of $\Delta t = 0.0157$. Figure 17 shows the relative amplitudes and frequencies of some selected modes. These 25 modes have the highest amplitudes and are associated with undamped eigenvalues. The frequency that is related to the hub vortex is $St_{hub} \simeq 0.34 \times f_r$ (Iungo et al., 2013). We expect that the hub vortex is associated with $St = 0.79$ shown in Fig. 17. Although $St_{BPf} = 7.62$ is the frequency that related are not associated with the highest amplitude, it still within the top 6% of amplitudes.

The eigenvalues that are associated with 25 modes lie on the unit circle, which indicates that the effect of these frequencies will not dissipate with the evolution of time as it is shown in Fig. 18. Both, PSD analysis and DMD show that $St_{BPf} = 7.62$ has an important role in the dynamic of the flow field.

Figure 19 shows the normalized streamwise and vertical velocities, u/U_∞ and v/U_∞. Figure 19(c) shows the spanwise vorticity $\omega_z D/U_\infty$, while Fig. 19(d) steamwise vorticity $\omega_x D/U_\infty$, respectively. The contour plots show clearly the tip vortices and hub vortex.

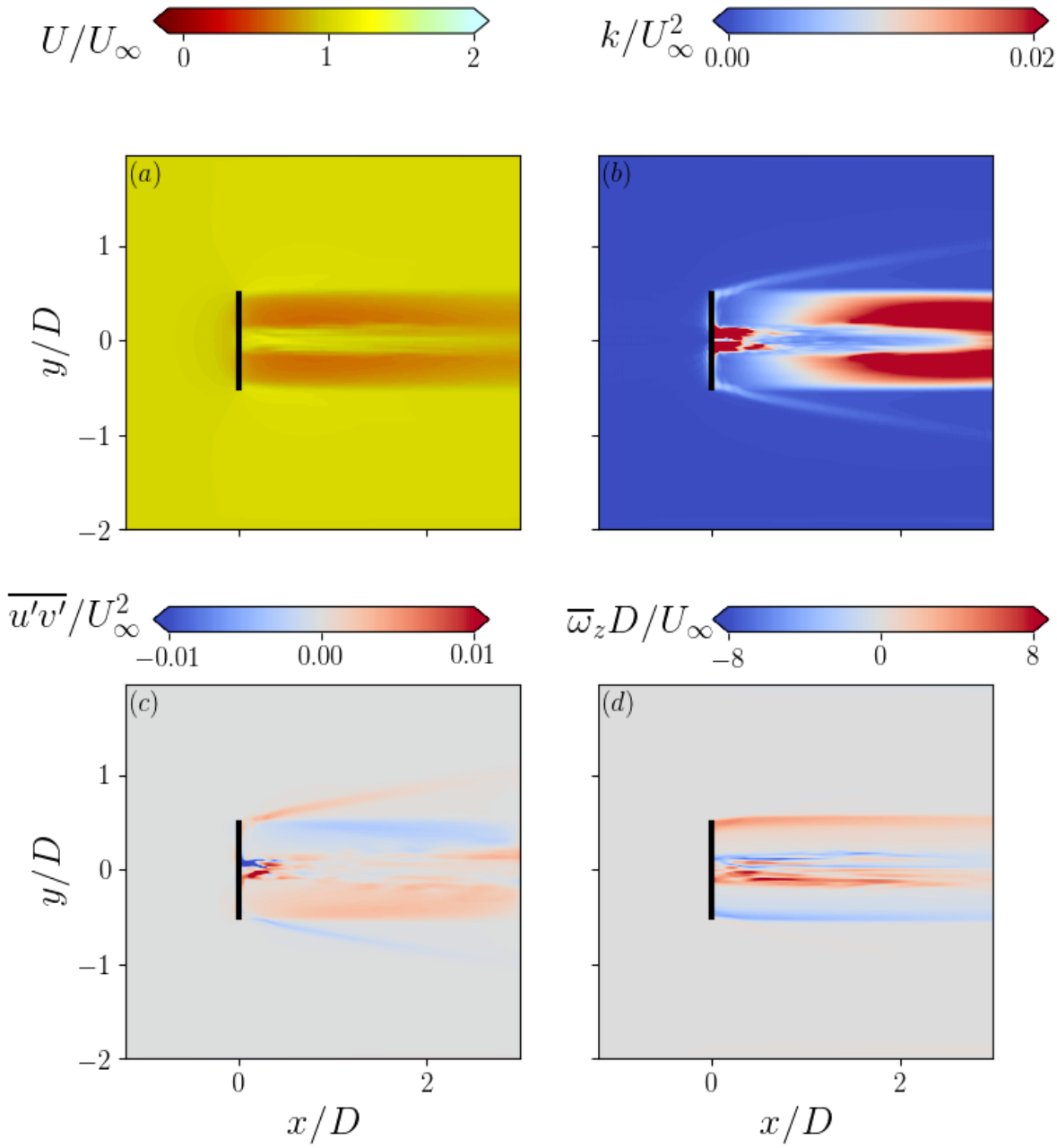

Figure 14: (a) The mean streamwise velocity U/U_∞, (b) turbulence kinetic energy k/U_∞, (c) vertical Reynolds shear stress $\overline{u'v'}/U_\infty$, and (d) mean spanwise vorticity $\omega_x D/U_\infty$, respectively.

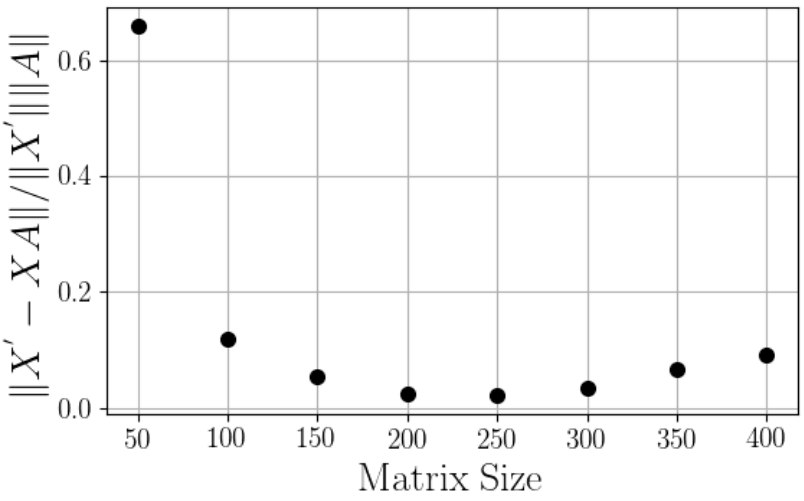

Figure 15: DMD residuals as a function of the number of snapshots.

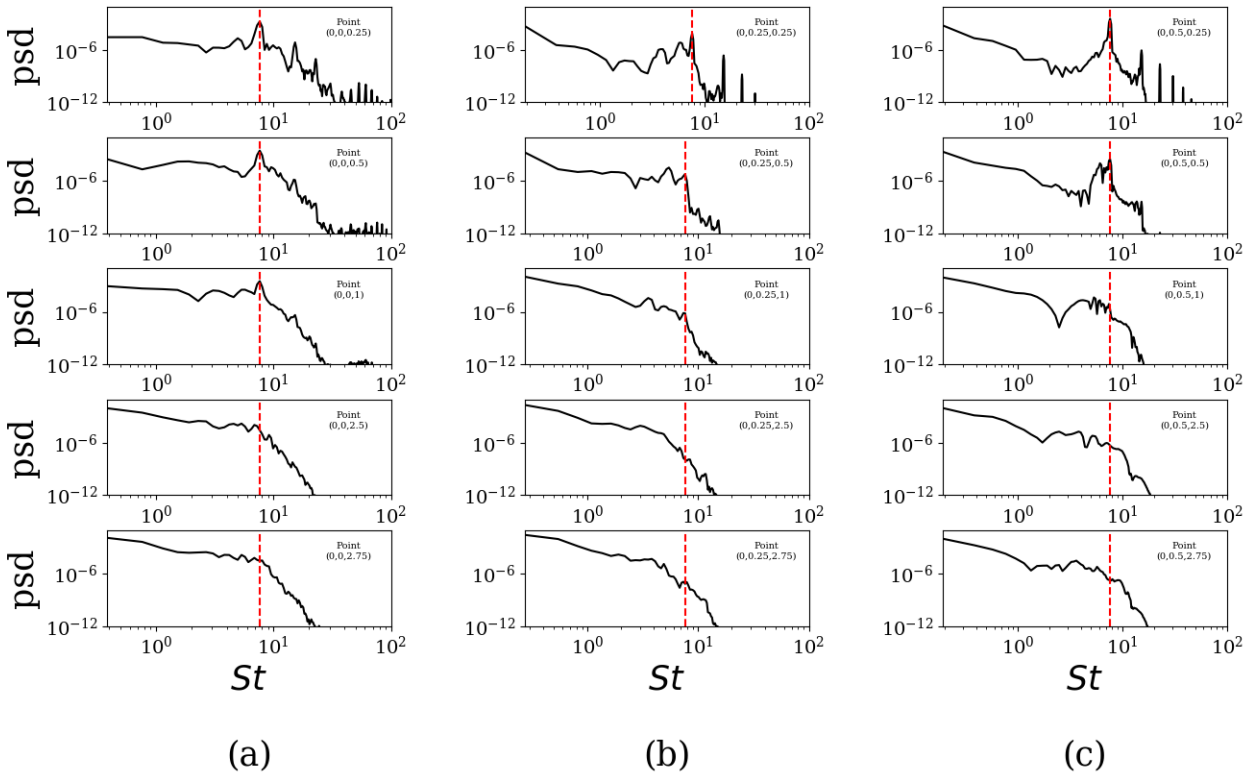

Figure 16: PSD as a function of St for (a) axial locations along the wind turbine centerline, (b) axial locations at $y/D = 0.25$, and (c) axial locations at $y/D = 0.55$

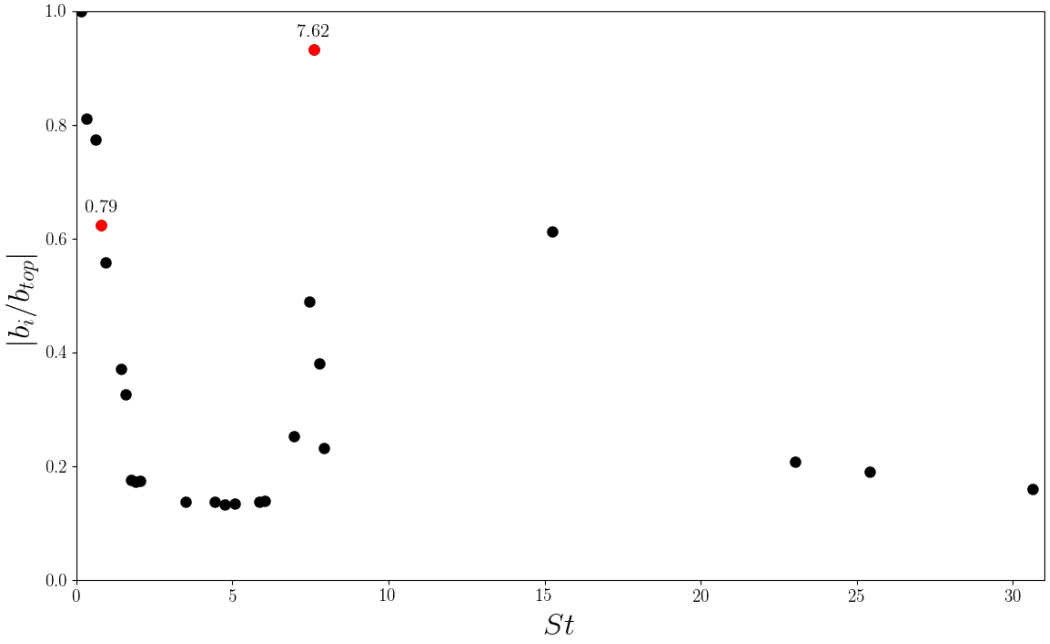

Figure 17: Relative amplitudes of most important 25 modes with their corresponding Strouhal number St. The red markers are the eigenvalues for frequencies $\mathrm{St}_{\mathrm{hub}} = 0.79$ and $\mathrm{St}_{\mathrm{BPf}} = 7.62$.

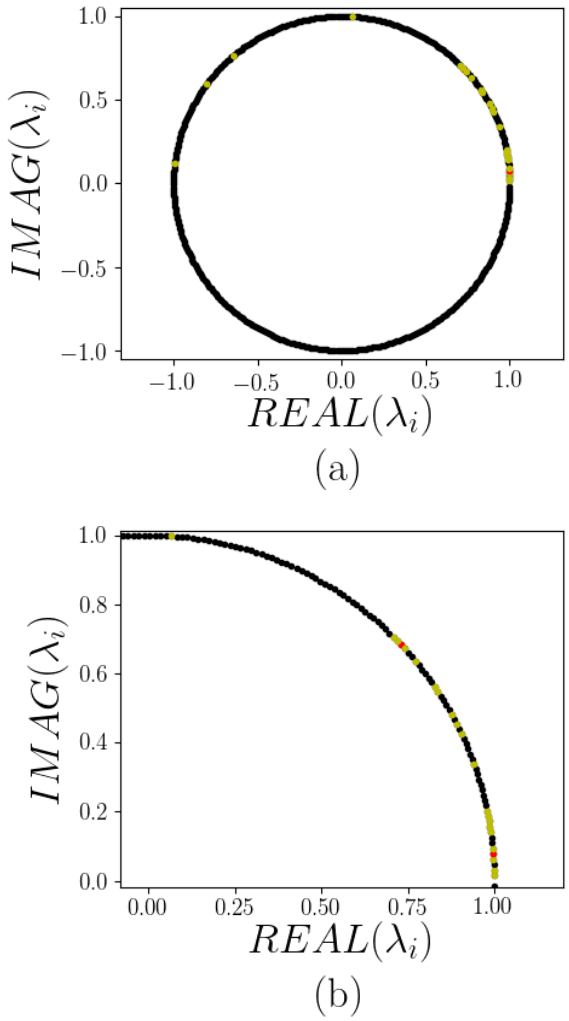

Figure 18: (a) Eigenvalues for the all 400 modes and their location relative to unit circle and (b) eigenvalues that are associated with the selected 25 modes. Eigenvalues that are associated with the selected 25 modes are in color. Red markers are the eigenvalues associated with frequencies; $\mathrm{St}_{\mathrm{hub}} = 0.79$ and $\mathrm{St}_{\mathrm{BPf}} = 7.62$, and yellow markers are the other selected 23 modes with the high amplitudes.

Table 2: Number of modes R and $\log_{10}(\gamma)$ value for each ROM.

$\log_{10}(\gamma)$	Number of Modes (R)
3.8	12
3.4	49
3.0	161
2.5	372

These are the coherent structures that govern the flow field, and they will be used to create the ROM.

To make the picture clear, Fig. 20 and Fig. 21 are contour plots of DMD modes that are related to $\mathrm{St_{BPf}} = 7.62$, while Fig. 22 and Fig. 23 show the mode of $\mathrm{St_{hub}} = 0.79$. In Figs. 21 and 23, frames (a),(b),(c) and (d) are cross-sections of the modes in yz-plane alone center plane after $x/D = 0.25$, 0.5, 1 and 2, respectively.

Sparsity-promoting DMD-based reduced order model

In this section, we apply the same approach for designing as ROM as used for the square cylinder case; different ROMs are created with different number of modes $R = 12, 49, 161$ and 372 to represent the flow field. Also, for these different ROMs, we analyze the relation between the R and the accuracy of our approximation. The relationship is studied by the performance parameters: reconstruction error RE and $\%loss$. The number of modes R in each ROM and the corresponding γ value are shown in Table 2.

Figure 24(a) shows the relation between γ and the $\%loss$, (b) shows the general relation between γ and R of each ROM. These shows slight fluctuation between γ values and both $\%loss$ and R, but it shows the same expected trend. Also, for the wind turbine wake the range of gamma values that give us an acceptable range of error is small $2.5 \leq \log_{10}(\gamma) \leq 3.5$. Table 2 is built based on this range.

First, to study each ROM, we search for the frequencies that have the highest amplitudes. Figure 25 shows the relative amplitudes and frequencies of some selected modes. From the this figure, we see that frequency $\mathrm{St_{BPf}} = 7.62$ has the highest amplitude in the four different

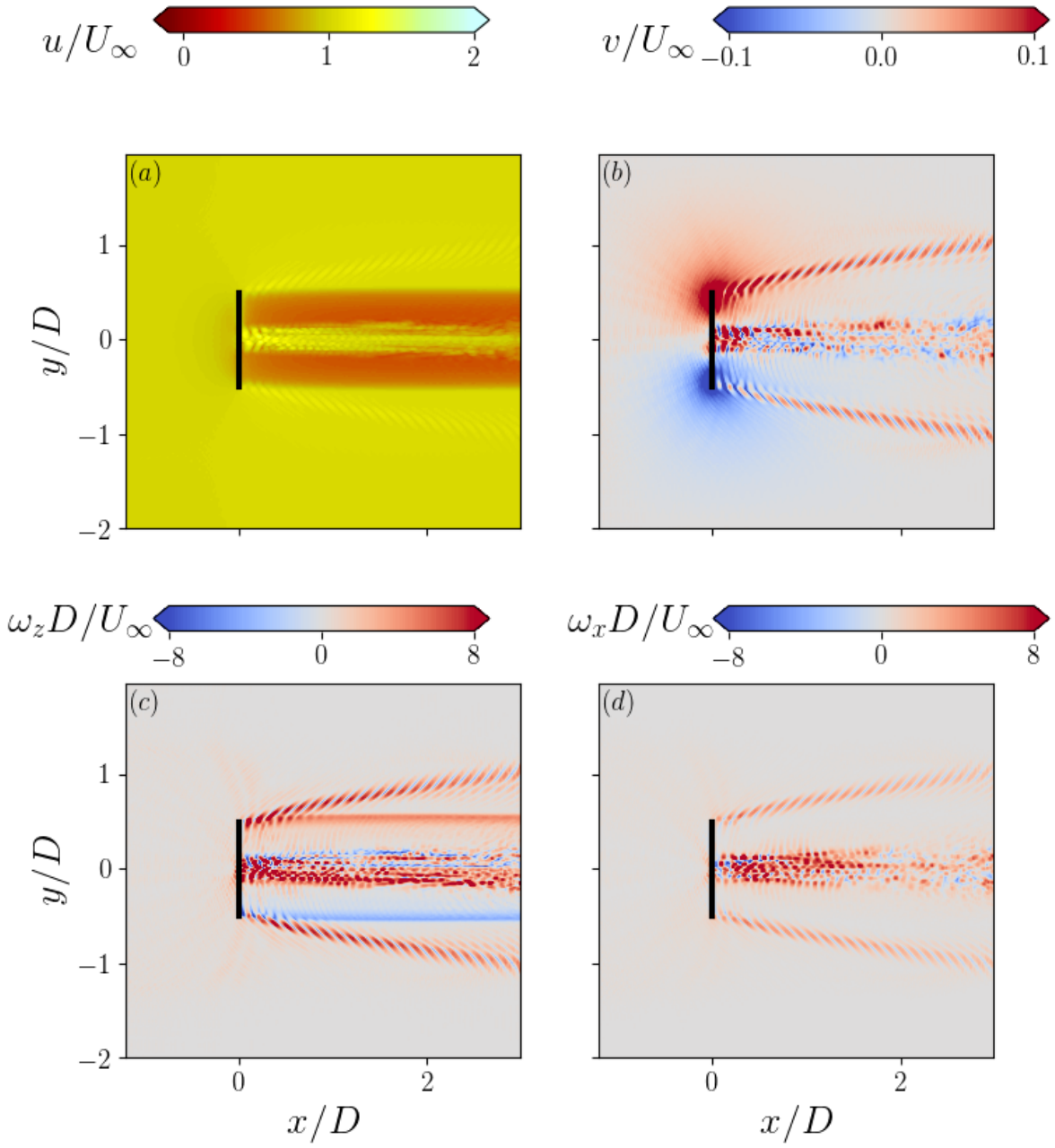

Figure 19: (a) The instantaneous streamwise velocity u/U_∞, (b) the vertical velocity v/U_∞, (c) the instantaneous spanwise vorticity $\omega_z D/U_\infty$, and (d) the instantaneous spanwise vorticity $\omega_x D/U_\infty$, respectively.

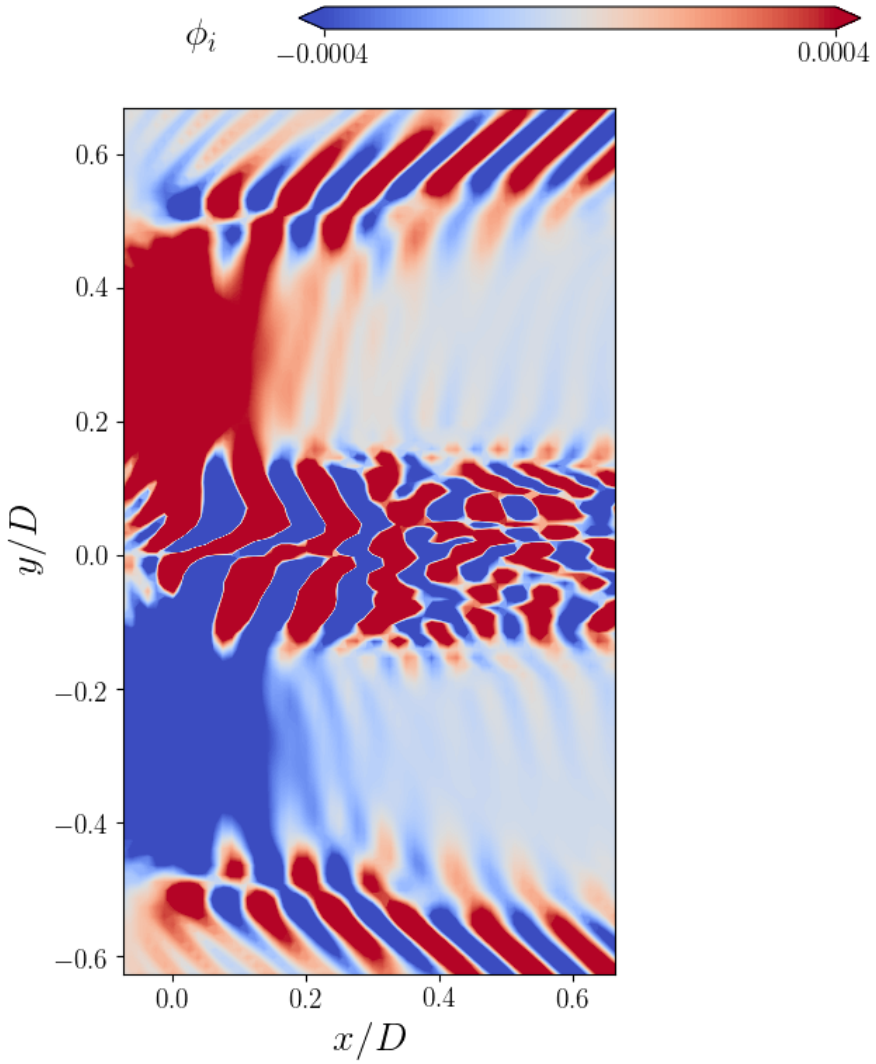

Figure 20: DMD mode related to $\mathrm{St}_{\mathrm{BPf}} = 7.62$ along the center plane.

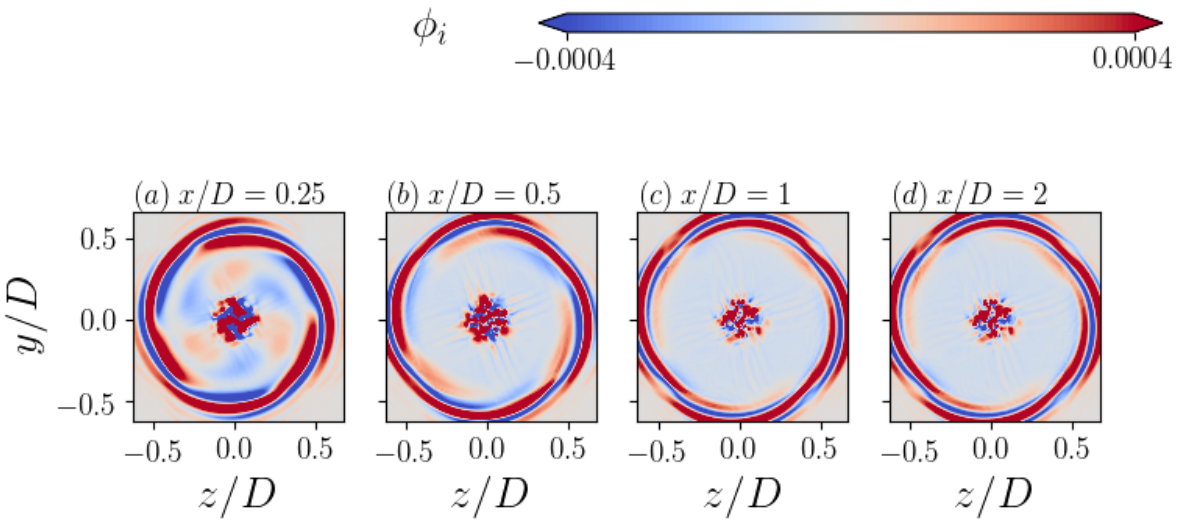

Figure 21: (a),(b),(c) and (d) are cross-sections of the mode related to $\mathrm{St_{BPf}} = 7.62$ of yz-plane alone center plane after (0.25D), (0.5D), (1D) and (2D), respectively.

ROMs. $\mathrm{St_{BPf}} = 7.62$ and $\mathrm{St_{hub}} = 0.79$ are colored in blue.

Figure 26 shows the eigenvalues for the all 400 modes and their location relative to unit circle. Eigenvalues that are associated with the selected ROM modes are identified. Figure 26 shows that these two frequencies are undamped.

Reconstruction error RE is calculated to test the quality of ROM with evolution of time. Figure 27 shows the RE for the four ROMs. The horizontal axes is the time over the period of the wind turbine rotor $T = 2pi/\omega$, where ω is the angular velocity. The RE decreases with increasing the the number of modes in the ROM. In general, all the ROM(s) show acceptable reconstruction error. They are expected increase in the reconstruction error after $t/T = 16$, where new times not used in the DMD begins. Figure 28 shows the relation between average value of reconstruction error RE_{avg} for different ROMs and the number modes R in the ROM.

Figures 29 to 32 show that the flow field is reconstructed. These figures show that the flow field is successfully reconstructed by the ROMs.

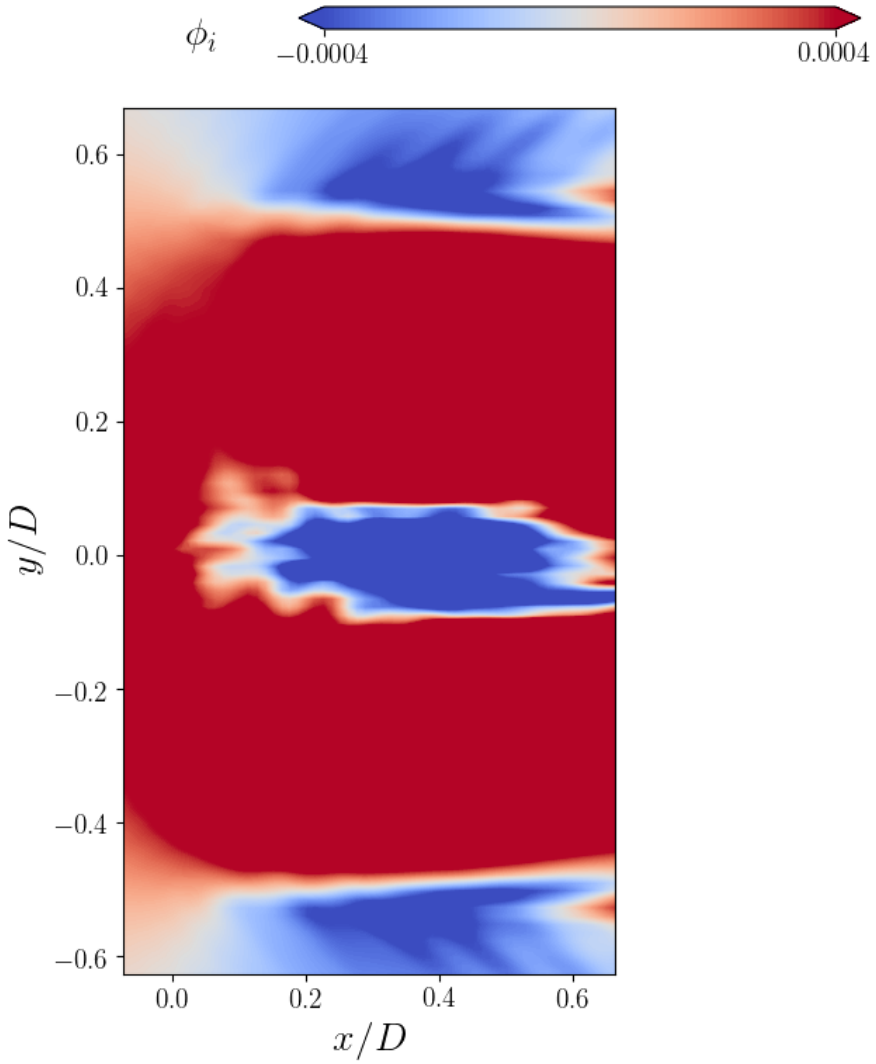

Figure 22: DMD mode related to $\mathrm{St}_{\mathrm{hub}} = 0.79$ along the center plane.

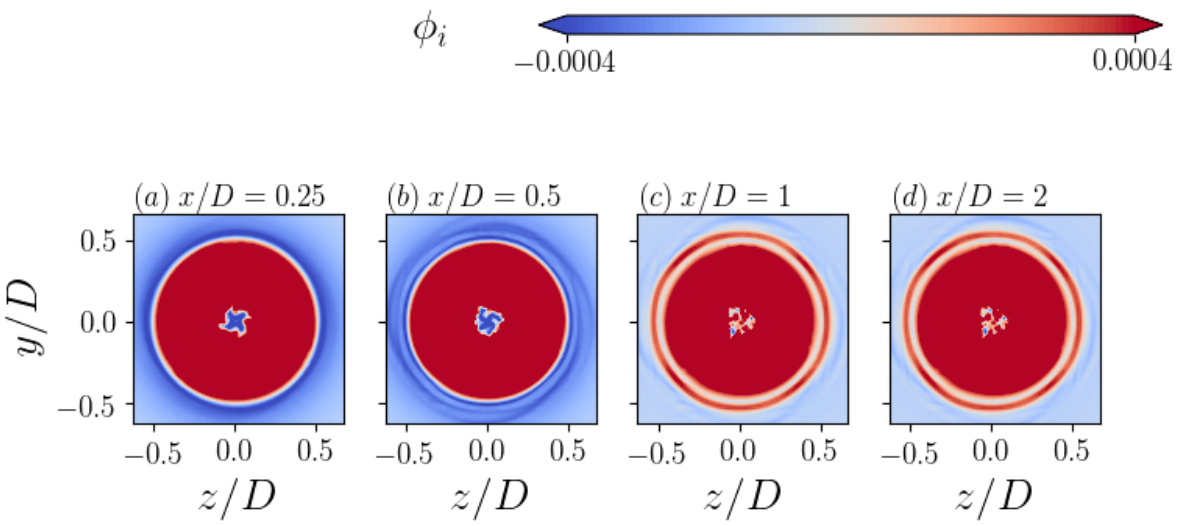

Figure 23: (a),(b),(c) and (d) are cross-sections of the mode related to $\mathrm{St}_{\mathrm{hub}} = 0.79$ of yz-plane alone center plane after (0.25D), (0.5D), (1D) and (2D), respectively.

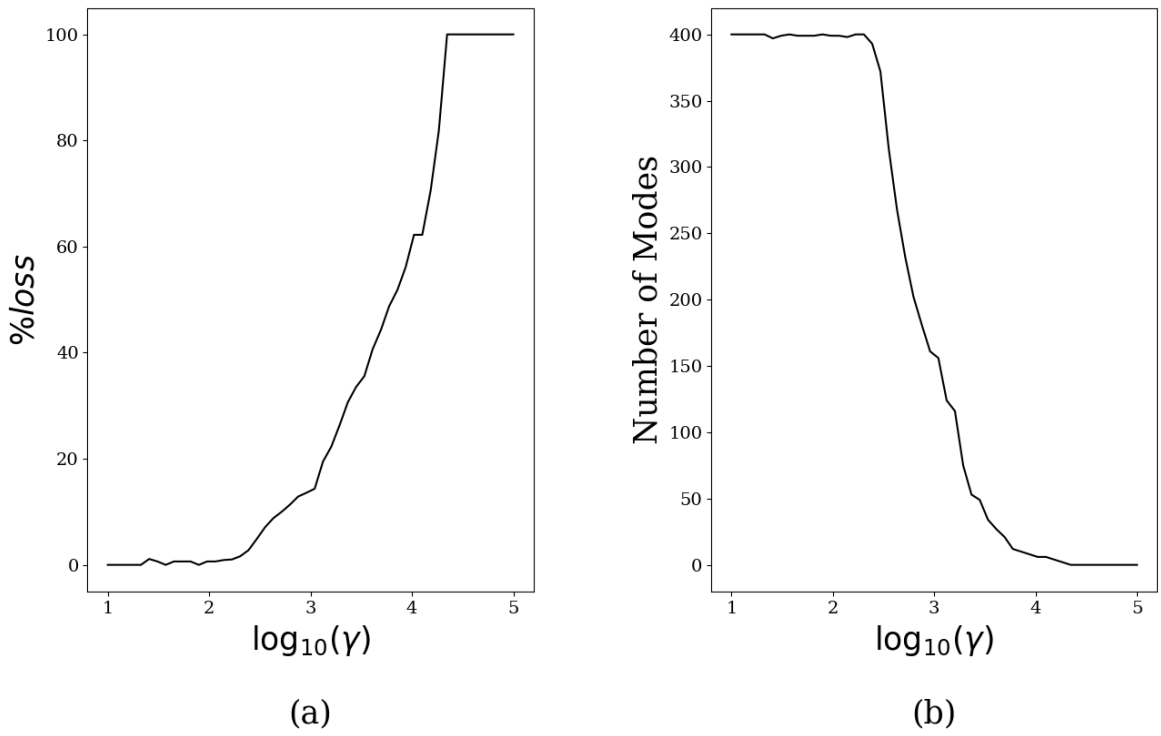

Figure 24: (a) The relation between γ and the $\%loss$, (b) the general relation between γ and the number of modes R of the ROM.

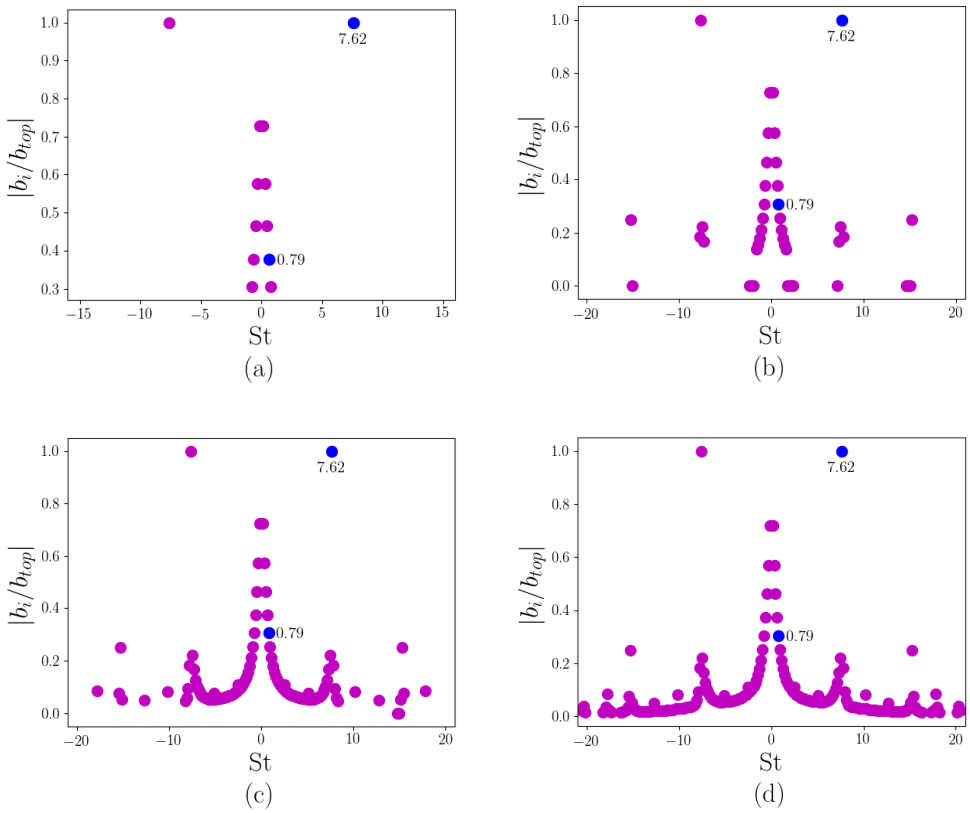

Figure 25: Relative amplitudes of three ROM(s) with the associated frequencies.(a) 12 modes, (b) 49 modes, (c) 161, and (d) 372 modes. The blue ones are the eigenvalues for frequencies; $\mathrm{St}_{\mathrm{BPF}} = 7.62$ and $\mathrm{St}_{\mathrm{hub}} = 0.79$.

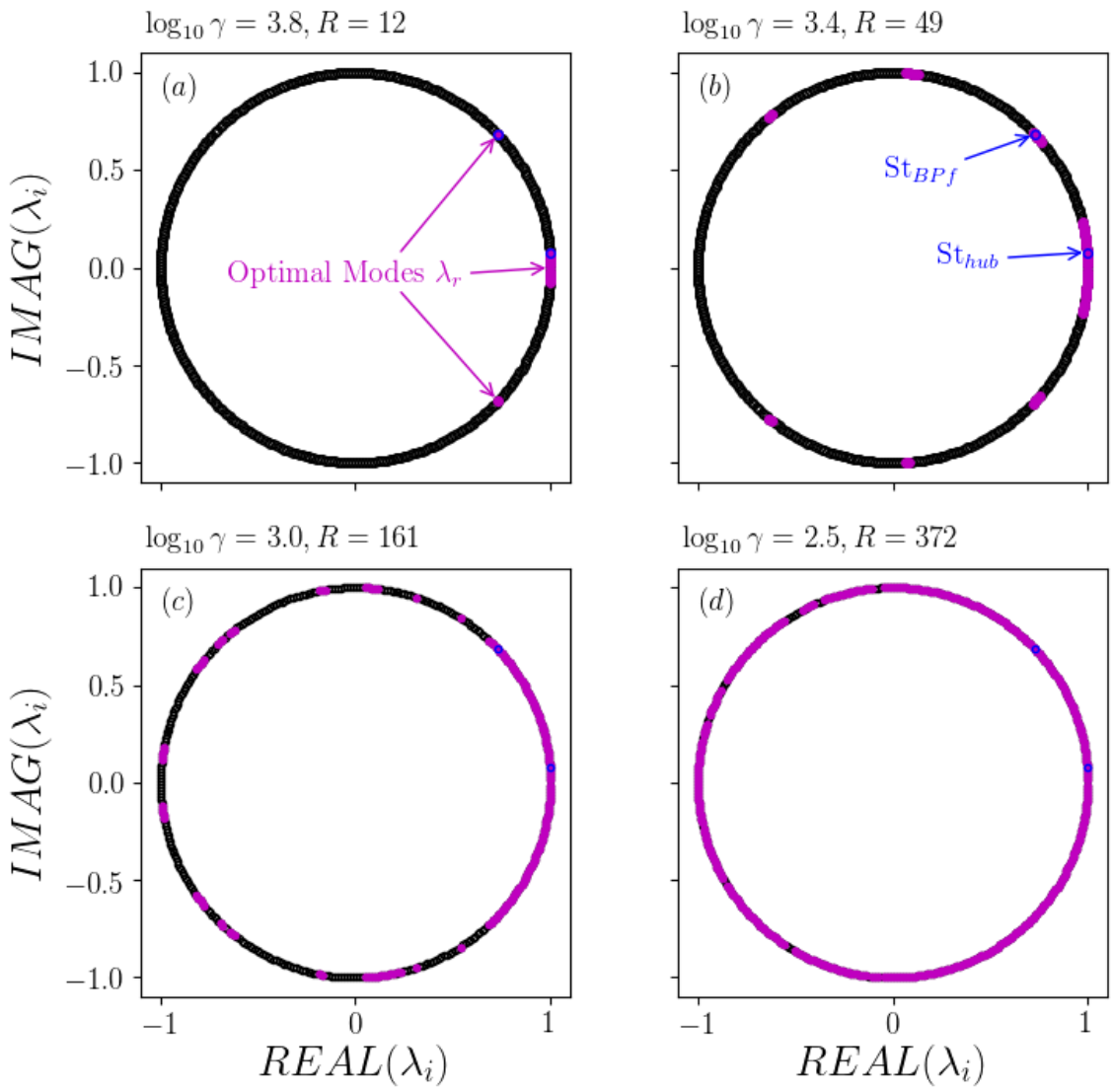

Figure 26: (a) Eigenvalues that are associated with the 12 modes ROM. (b), (c) and (d) eigenvalues that are associated with the ROM of ; 49, 161 and 372 modes, respectively.

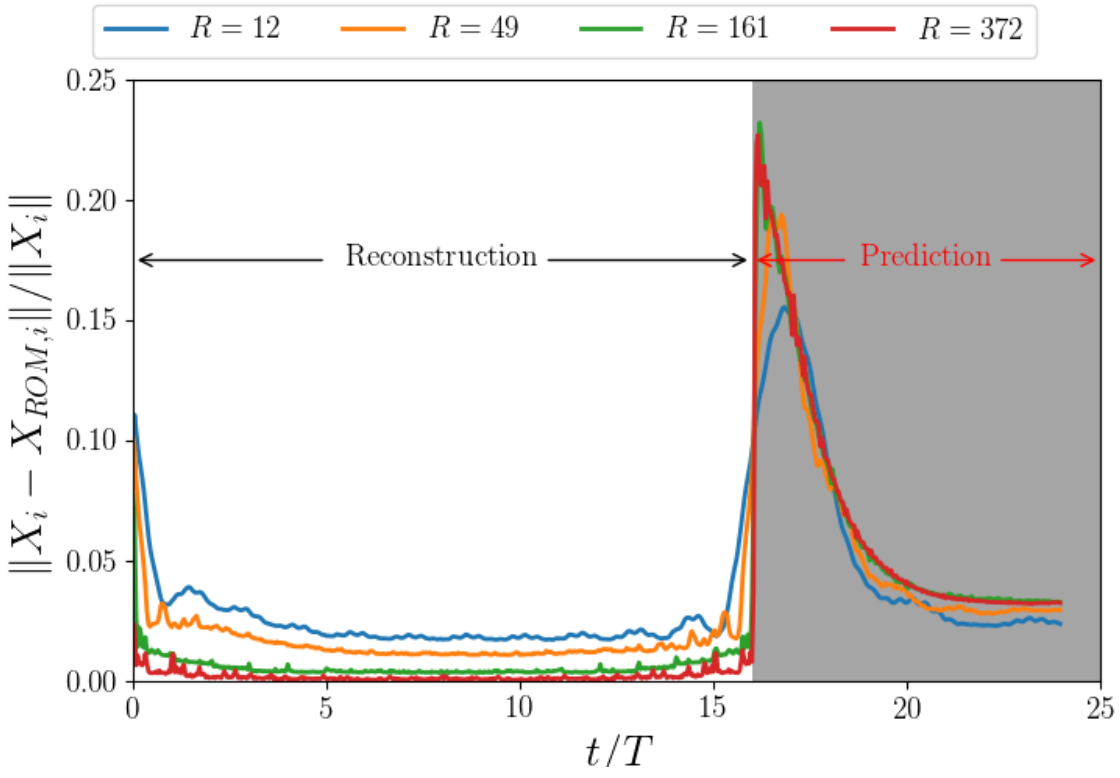

Figure 27: Reconstruction Error RE for the four ROM(s).

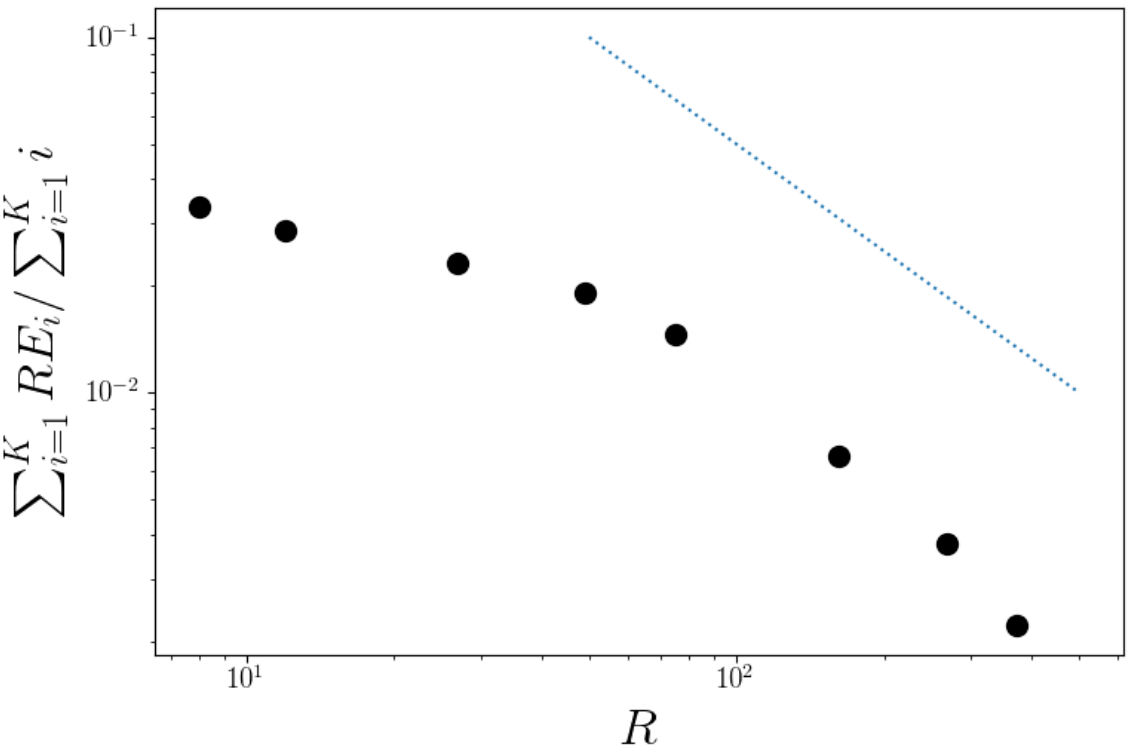

Figure 28: Average Value of Reconstruction Error RE_{avg} and the Number of ROM Modes R.

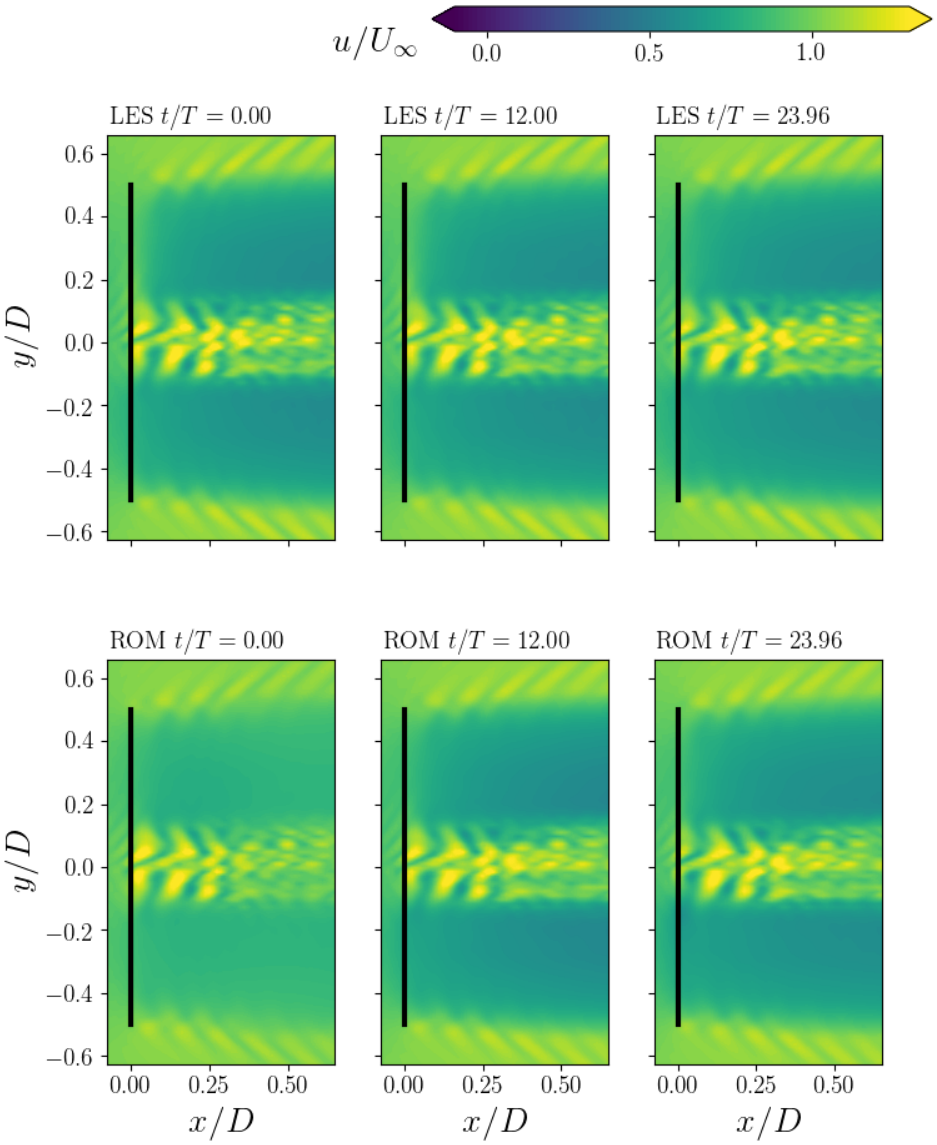

Figure 29: Contour of streamwise velocity of the wake for the actual flow and the reconstruction wake with 12 modes at different times. The top plot is the streamwise velocity of the actual flow, while the bottom is the streamwise velocity of the ROM.

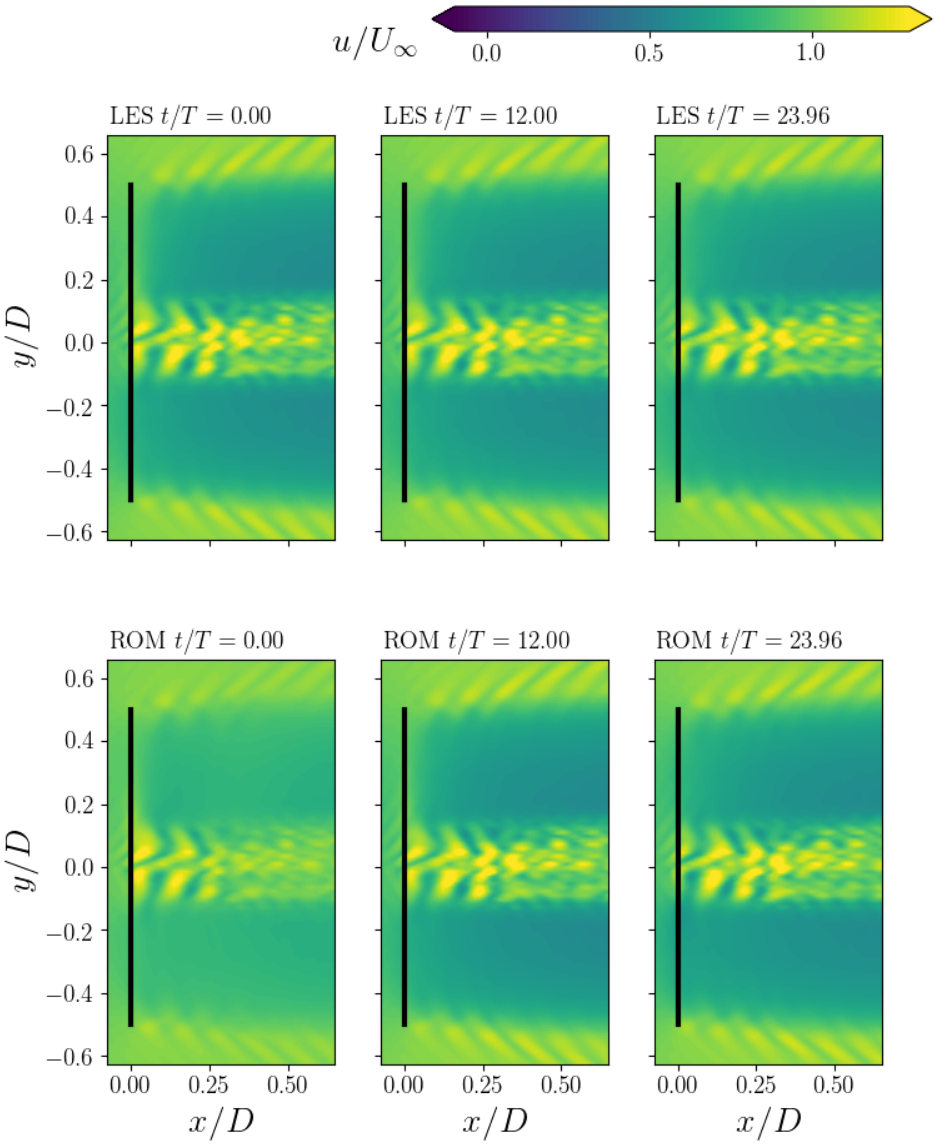

Figure 30: Contour of streamwise velocity of the wake for the actual flow and the reconstruction wake with 49 modes at different times. The top plot is the streamwise velocity of the actual flow, while the bottom is the streamwise velocity of the ROM.

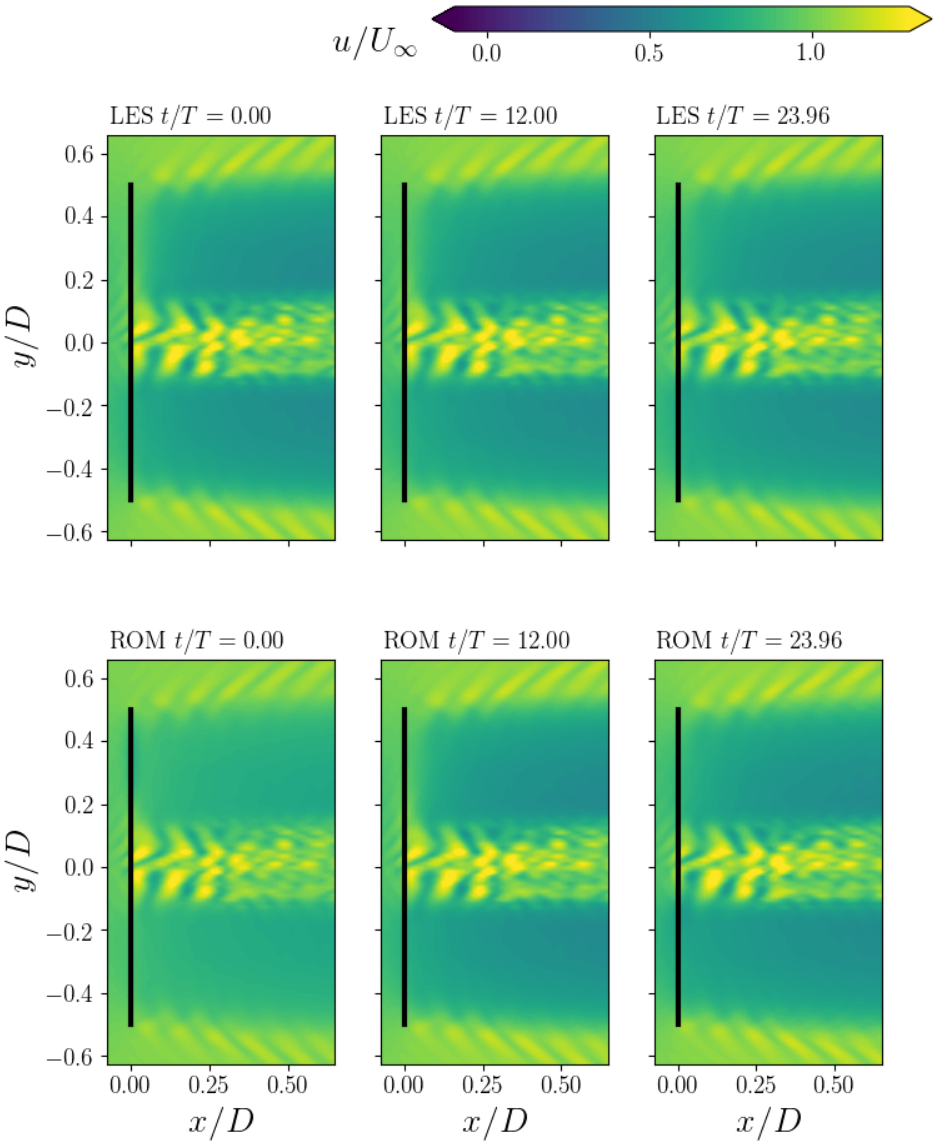

Figure 31: Contour of streamwise velocity of the wake for the actual flow and the reconstruction wake with 132 modes at different times. The top plot is the streamwise velocity of the actual flow, while the bottom is the streamwise velocity of the ROM.

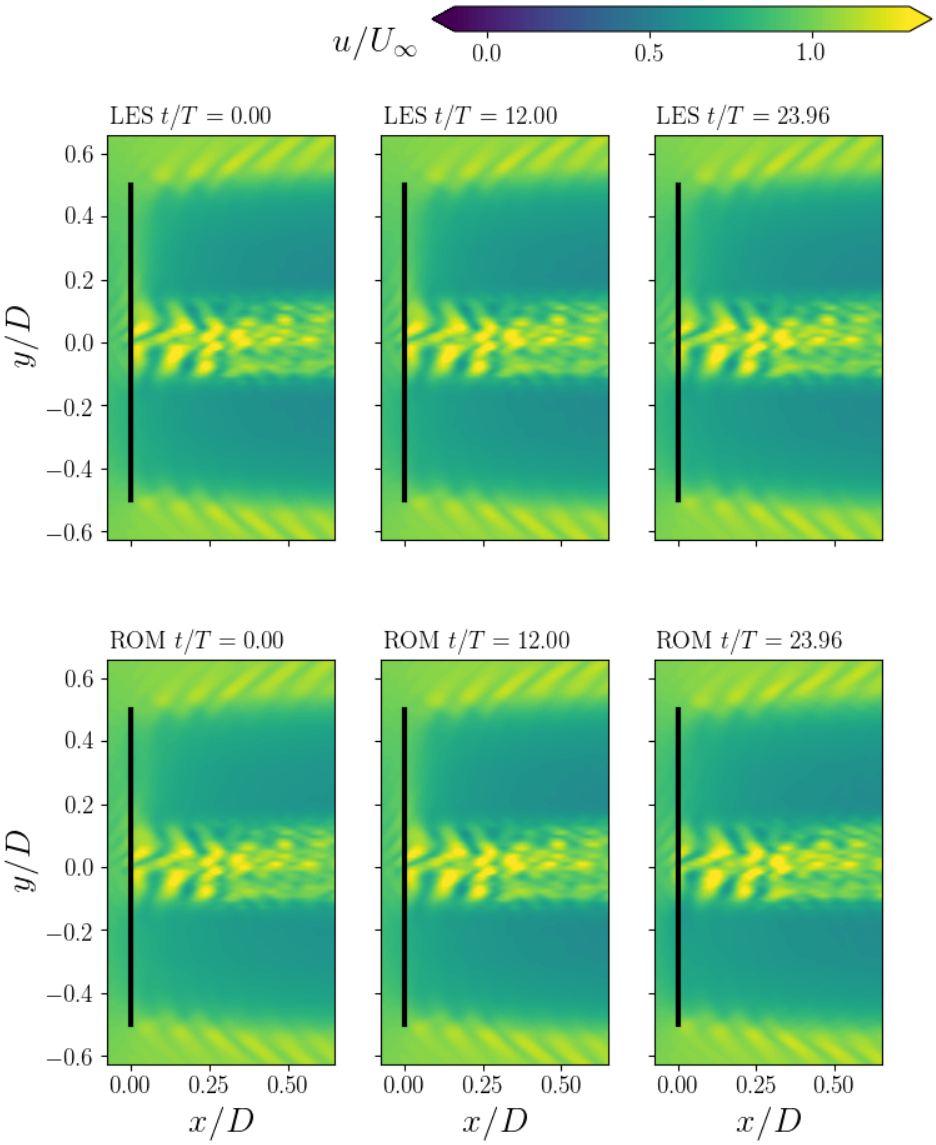

Figure 32: Contour of streamwise velocity of the wake for the actual flow and the reconstruction wake with 372 modes at different times. The top plot is the streamwise velocity of the actual flow, while the bottom is the streamwise velocity of the ROM.

CHAPTER 5

Summary and Conclusions

A model for wind turbine wakes is developed using DMD by reduction and careful selection of the spatial modes. Several methods are considered for mode selection: a user-intuition based on the amplitude value of modes and a sparse sensing. The former method has been demonstrated in Iungo et al. (2015), but the number of modes employed can be considerable high. DMD is able to capture modes that are directly related to the wake instabilities and maintain frequencies similar to those found in simulations and experimental measurements. In the user-intuition based method a DMD-based ROM designed with carefully selected 975 modes with high amplitudes and undamped effects. Sparsity-promoting DMD algorithm employing sparse sensing is demonstrated to select a significant subset of the DMD modes to build accurate ROMs. The error of the ROM is shown to be linearly dependent on the number of modes selected.

A large-eddy simulation of a wind turbine with a uniform inflow is performed and used to build a DMD-based model. Physical key features of the flow field including the tip vortices and hub vortex are identified with DMD. These two coherent structures have relatively the highest amplitudes compared to all modes. Sparse sampling of the the DMD modes, reveals that modes related to these coherent structures are always selected even with the number of modes is less than 10 out of a maximum of 400 modes. Models designed with the optimal amplitudes using the sparsity-promoting DMD algorithm are shown to be nearly independent of the number of modes when less than 10% of the modes are selected. The maximum reconstruction error is less than 10% compared with the simulation results. The dynamic model is able to capture the unsteady motions of the tip vortices and hub vortex. Furthermore, in the prediction phase, where the time is incremented past the last data point used to create the model, the error is shown to exponentially decrease. This is due to the periodic nature of the wind turbine wake.

In future work, more complex cases will be considered. Large-eddy simulation of non-uniform incoming velocity, such as an atmospheric boundary layer, will be performed as well

as higher fidelity modeling of the wind turbine including the nacelle geometry. Using the DMD-based, a model of an entire wind farm can be sought. This comprehensive model will be able to predicted the total power output and its variability of a wind farm. This will allow for optimization and uncertainty quantification of a wind farm power output, which can lead to enhance design criteria and improved levelized cost of energy for wind farms.

REFERENCES

U.S. Energy Information Administration. *Annual Energy Outlook 2019 with projections to 2050*. Government Printing Office, 2019.

A Crespo, J Hernandez, and S Frandsen. Survey of modelling methods for wind turbine wakes and wind farms. *Wind Energy*, 2(1):1–24, 1999.

Richard JAM Stevens and Charles Meneveau. Flow structure and turbulence in wind farms. *Annual Review of Fluid Mechanics*, 49, 2017.

Niels Otto Jensen. *A note on wind generator interaction*. Risø National Laboratory, 1983.

Majid Bastankhah and Fernando Porté-Agel. A new analytical model for wind-turbine wakes. *Renewable Energy*, 70:116–123, 2014.

PBS Lissaman. Energy effectiveness of arbitrary arrays of wind turbines. *Journal of Energy*, 3(6):323–328, 1979.

Sten Frandsen. On the wind speed reduction in the center of large clusters of wind turbines. *Journal of Wind Engineering and Industrial Aerodynamics*, 39(1):251–265, 1992.

Sten Frandsen, Rebecca Barthelmie, Sara Pryor, Ole Rathmann, Søren Larsen, Jørgen Højstrup, and Morten Thøgersen. Analytical modelling of wind speed deficit in large offshore wind farms. *Wind energy*, 9(1-2):39–53, 2006.

Marc Calaf, Charles Meneveau, and Johan Meyers. Large eddy simulation study of fully developed wind-turbine array boundary layers. *Physics of Fluids*, 22(1):015110, 2010.

I Katic, Jørgen Højstrup, and Niels Otto Jensen. A simple model for cluster efficiency. In *European wind energy association conference and exhibition*, volume 1, pages 407–410, 1986.

Xiaolei Yang, Seokkoo Kang, and Fotis Sotiropoulos. Computational study and modeling of turbine spacing effects in infinite aligned wind farms. *Physics of Fluids*, 24(11):115107, 2012.

Gunner C Larsen, Helge Aa Madsen, Kenneth Thomsen, and Torben J Larsen. Wake meandering: a pragmatic approach. *Wind Energy*, 11(4):377–395, 2008.

H Aa Madsen, Gunner Chr Larsen, Torben J Larsen, Niels Troldborg, and R Mikkelsen. Calibration and validation of the dynamic wake meandering model for implementation in an aeroelastic code. *Journal of Solar Energy Engineering*, 132(4):041014, 2010.

Davide Medici and PH Alfredsson. Measurements on a wind turbine wake: 3d effects and bluff body vortex shedding. *Wind Energy: An International Journal for Progress and Applications in Wind Power Conversion Technology*, 9(3):219–236, 2006.

D Medici and P Henrik Alfredsson. Measurements behind model wind turbines: further evidence of wake meandering. *Wind Energy: An International Journal for Progress and Applications in Wind Power Conversion Technology*, 11(2):211–217, 2008.

ValeryL Okulov, IgorV Naumov, RobertF Mikkelsen, IvanK Kabardin, and JensN Sørensen. A regular strouhal number for large-scale instability in the far wake of a rotor. *Journal of Fluid Mechanics*, 747:369, 2014.

Daniel Foti, Xiaolei Yang, Michele Guala, and Fotis Sotiropoulos. Wake meandering statistics of a model wind turbine: Insights gained by large eddy simulations. *Physical Review Fluids*, 1(4):044407, 2016.

Xiaolei Yang and Fotis Sotiropoulos. Wake characteristics of a utility-scale wind turbine under coherent inflow structures and different operating conditions. *Physical Review Fluids*, 4(2):024604, 2019.

Daniel Foti, Xiaolei Yang, Lian Shen, and Fotis Sotiropoulos. Effect of wind turbine nacelle on turbine wake dynamics in large wind farms. *Journal of Fluid Mechanics*, 869:1–26, 2019.

NE Joukowski. Vortex theory of a rowing screw. *Trudy otdeleniya fizicheskikh nauk obshchestva lubitelei estestvoznaniya*, 16(1):1–31, 1912.

Leonardo P Chamorro and Fernando Porté-Agel. A wind-tunnel investigation of wind-turbine wakes: boundary-layer turbulence effects. *Boundary-layer meteorology*, 132(1):129–149, 2009.

Hui Hu, Zifeng Yang, and P. P. Sarkar. Dynamic wind loads and wake characteristics of a wind turbine model in an atmospheric boundary layer wind. *Experiments in Fluids*, 52: 1277–1294, 2012.

Stefan Ivanell, Jens N Sørensen, Robert Mikkelsen, and Dan Henningson. Analysis of numerically generated wake structures. *Wind Energy: An International Journal for Progress and Applications in Wind Power Conversion Technology*, 12(1):63–80, 2009.

Niels Troldborg, Jens N Sørensen, and Robert Mikkelsen. Actuator line simulation of wake of wind turbine operating in turbulent inflow. In *J. Phys. Conf. Ser*, volume 75, pages 1–012063, 2007.

Sheila E Widnall. The stability of a helical vortex filament. *Journal of Fluid Mechanics*, 54 (4):641–663, 1972.

Maroi Felli, Roberto Camussi, and F Di Felice. Mechanisms of evolution of the propeller wake in the transition and far fields. *Journal of Fluid Mechanics*, 682:5, 2011.

Seokkoo Kang, Xiaolei Yang, and Fotis Sotiropoulos. On the onset of wake meandering for an axial flow turbine in a turbulent open channel flow. *Journal of Fluid Mechanics*, 744: 376–403, 2014.

Daniel Foti, Xiaolei Yang, Filippo Campagnolo, David Maniaci, and Fotis Sotiropoulos. Wake meandering of a model wind turbine operating in two different regimes. *Physical Review Fluids*, 3(5):054607, 2018a.

Giacomo Valerio Iungo, Francesco Viola, Simone Camarri, Fernando Porté-Agel, and François Gallaire. Linear stability analysis of wind turbine wakes performed on wind tunnel measurements. *Journal of Fluid Mechanics*, 737:499–526, 2013.

Francesco Viola, Giacomo Valerio Iungo, Simone Camarri, Fernando Porté-Agel, and Francois Gallaire. Prediction of the hub vortex instability in a wind turbine wake: stability analysis with eddy-viscosity models calibrated on wind tunnel data. *Journal of Fluid Mechanics*, 750, 2014.

Daniel Foti, Xiaolei Yang, and Fotis Sotiropoulos. Similarity of wake meandering for different wind turbine designs for different scales. *Journal of Fluid Mechanics*, 842:5–25, 2018b.

LP Chamorro, C Hill, S Morton, Christopher Ellis, REA Arndt, and Fotis Sotiropoulos. On the interaction between a turbulent open channel flow and an axial-flow turbine. *Journal of Fluid Mechanics*, 716:658–670, 2013.

Philip Holmes, John L Lumley, Gahl Berkooz, and Clarence W Rowley. *Turbulence, coherent structures, dynamical systems and symmetry*. Cambridge University Press, 2012.

Peter J Schmid. Dynamic mode decomposition of numerical and experimental data. *Journal of Fluid Mechanics*, 656:5–28, 2010.

J Nathan Kutz, Steven L Brunton, Bingni W Brunton, and Joshua L Proctor. *Dynamic mode decomposition: data-driven modeling of complex systems*. SIAM, 2016.

Krithika Manohar, Bingni W Brunton, J Nathan Kutz, and Steven L Brunton. Data-driven sparse sensor placement for reconstruction: Demonstrating the benefits of exploiting known patterns. *IEEE Control Systems*, 38(3):63–86, 2018.

David L Donoho. Compressed sensing. *IEEE Transactions on Information Theory*, 52(4): 1289–1306, 2006.

James E Fowler. Compressive-projection principal component analysis. *IEEE Transactions on Image Processing*, 18(10):2230–2242, 2009.

Richard G Baraniuk, Volkan Cevher, Marco F Duarte, and Chinmay Hegde. Model-based compressive sensing. *IEEE Transactions on Information Theory*, 56(4):1982–2001, 2010.

Ido Bright, Guang Lin, and J Nathan Kutz. Compressive sensing based machine learning strategy for characterizing the flow around a cylinder with limited pressure measurements. *Physics of Fluids*, 25(12):127102, 2013.

Zlatko Drmac and Serkan Gugercin. A new selection operator for the discrete empirical interpolation method—improved a priori error bound and extensions. *SIAM Journal on Scientific Computing*, 38(2):A631–A648, 2016.

Daniel Foti, Sven Giorno, and Karthik Duraisamy. An adaptive mesh refinement approach based on optimal sparse sensing. *Theoretical and Computational Fluid Dynamics*, pages 1–26, 2020.

Mihailo R Jovanović, Peter J Schmid, and Joseph W Nichols. Sparsity-promoting dynamic mode decomposition. *Physics of Fluids*, 26(2):024103, 2014.

Sasan Sarmast, Reza Dadfar, Robert F Mikkelsen, Philipp Schlatter, Stefan Ivanell, Jens N Sørensen, and Dan S Henningson. Mutual inductance instability of the tip vortices behind a wind turbine. *Journal of Fluid Mechanics*, 755:705–731, 2014.

Mithu Debnath, Christian Santoni, Stefano Leonardi, and Giacomo Valerio Iungo. Towards reduced order modelling for predicting the dynamics of coherent vorticity structures within wind turbine wakes. *Philosophical Transactions of the Royal Society A: Mathematical, Physical and Engineering Sciences*, 375(2091):20160108, 2017.

Liang Ge and Fotis Sotiropoulos. A numerical method for solving the 3d unsteady incompressible navier–stokes equations in curvilinear domains with complex immersed boundaries. *Journal of Computational Physics*, 225(2):1782–1809, 2007.

Anvar Gilmanov and Fotis Sotiropoulos. A hybrid cartesian/immersed boundary method for simulating flows with 3d, geometrically complex, moving bodies. *Journal of Computational Physics*, 207(2):457–492, 2005.

Joseph Smagorinsky. General circulation experiments with the primitive equations: I. the basic experiment. *Monthly Weather Review*, 91(3):99–164, 1963.

Massimo Germano, Ugo Piomelli, Parviz Moin, and William H Cabot. A dynamic subgrid-scale eddy viscosity model. *Physics of Fluids*, 3(7):1760–1765, 1991.

Seokkoo Kang, Iman Borazjani, Jonathan A Colby, and Fotis Sotiropoulos. Numerical simulation of 3d flow past a real-life marine hydrokinetic turbine. *Advances in Water Resources*, 39:33–43, 2012.

Clarence W Rowley, Igor Mezić, Shervin Bagheri, Philipp Schlatter, and Dan S Henningson. Spectral analysis of nonlinear flows. *Journal of fluid mechanics*, 641:115–127, 2009.

Atul Sharma and V Eswaran. Heat and fluid flow across a square cylinder in the two-dimensional laminar flow regime. *Numerical Heat Transfer, Part A: Applications*, 45(3): 247–269, 2004.

Ahmad Sohankar, C Norberg, and L Davidson. Simulation of three-dimensional flow around a square cylinder at moderate reynolds numbers. *Physics of fluids*, 11(2):288–306, 1999.

Xiaolei Yang, Jiarong Hong, Matthew Barone, and Fotis Sotiropoulos. Coherent dynamics in the rotor tip shear layer of utility-scale wind turbines. *Journal of Fluid Mechanics*, 804: 90–115, 2016.

Jens Norkær Sorensen and Wen Zhong Shen. Numerical modeling of wind turbine wakes. *J. Fluids Eng.*, 124(2):393–399, 2002.

Xiaolei Yang, Fotis Sotiropoulos, Robert J Conzemius, John N Wachtler, and Mike B Strong. Large-eddy simulation of turbulent flow past wind turbines/farms: the Virtual Wind Simulator (VWiS). *Wind Energy*, 18(12):2025–2045, 2015.

Giacomo V Iungo, Christian Santoni-Ortiz, Mahdi Abkar, Fernando Porté-Agel, Mario A Rotea, and Stefano Leonardi. Data-driven reduced order model for prediction of wind turbine wakes. In *Journal of Physics: Conference Series*, volume 625, page 012009. IOP Publishing, 2015.

APPENDIX A

b- AND β-Minimization Steps

- b-MINIMIZATION STEP: Jovanović et al. (2014) shows that the b-minimization step in Eqn. (23) can be presented as:

$$\underset{b}{\text{minimize}} \quad J(b) + \frac{\rho}{2}\|b - u^k\|_F^2$$

where,

$$u^k = \beta^k - \frac{1}{\rho}\mu^k$$

Using Eqn. (18):

$$\underset{b}{\text{minimize}} \quad b^*(P + (\frac{\rho}{2})I)b - (q + (\frac{\rho}{2})u^k)^*b - b^*(q + (\frac{\rho}{2})u^k + s + \|u^k\|_2^2,$$

So, the b-minimization:

$$b^{k+1} = (P + (\frac{\rho}{2})I)^{-1}(q + (\frac{\rho}{2})u^k)$$

- β-MINIMIZATION STEP: Jovanović et al. (2014) shows that the β-minimization step in Eqn. (24) can be presented as:

$$\underset{\beta}{\text{minimize}} \quad \gamma g(b) + \frac{\rho}{2}\|\beta - \nu^k\|_F^2$$

where,

$$\nu^k = b^{k+1} + \frac{1}{\rho}\mu^k$$

So, the β-minimization:

$$\beta_i^{k+1} = S_K(v_i^k) + \frac{1}{\rho}\mu^k, \quad K = \gamma/\rho$$

where, $S_K(.)$ is the soft thresholding operator:

$$S_K(v_i^k) = \begin{cases} \nu_i^k - K, & \nu_i^k > K, \\ 0, & \nu_i^k \in [-K, K], \\ \nu_i^k + K, & \nu_i^k < -K \end{cases}$$

APPENDIX B

The Algorithm for Solving Eqn. (21)

Jovanović et al. (2014) shows that the Eqn. (21) can be presented as:

$$\begin{bmatrix} P & E \\ E^T & 0 \end{bmatrix} \begin{bmatrix} b \\ \nu \end{bmatrix} = \begin{bmatrix} q \\ 0 \end{bmatrix}$$

So that, the optimal amplitudes vector b_{sp} can be computed by:

$$b_{sp} = \begin{bmatrix} I & 0 \end{bmatrix} \begin{bmatrix} P & E \\ E^T & 0 \end{bmatrix}^{-1} \begin{bmatrix} q \\ 0 \end{bmatrix}$$